JGR Solid Earth

RESEARCH ARTICLE
10.1029/2018JB017221

Magnetotelluric Apparent Resistivity Tensors for Improved Interpretations and 3-D Inversions

P. Hering[1], **C. Brown**[2], **and A. Junge**[1]

[1]Institute of Geosciences, Goethe-Universität Frankfurt, Frankfurt am Main, Germany, [2]Ryan Institute, National University of Ireland, Galway, Ireland

Key Points:
- Properties of apparent resistivity tensors in multidimensional environments are explained using EM induction theory
- Apparent resistivity tensor and apparent resistivity phase tensor have high sensitivity to horizontal and vertical resistivity gradients
- A 3-D inversion study shows improvements in resolving boundaries and structures using the new tensors

Supporting Information:
- Supporting Information S1

Correspondence to:
P. Hering,
phhering@geophysik.uni-frankfurt.de

Citation:
Hering, P., Brown, C., & Junge, A. (2019). Magnetotelluric apparent resistivity tensors for improved interpretations and 3-D inversions. *Journal of Geophysical Research: Solid Earth*, *124*, 7652–7679. https://doi.org/10.1029/2018JB017221

Received 19 DEC 2018
Accepted 18 JUL 2019
Accepted article online 25 JUL 2019
Published online 24 AUG 2019

The copyright line for this article was changed on 25 NOV 2020 after original online publication. Projekt Deal funding statement has been added.

Abstract The complex magnetotelluric (MT) apparent resistivity tensor can be decomposed into two real tensors, the apparent resistivity and the resistivity phase tensors, which represent relationships between the observed electric field at a point on the Earth's surface and an associated apparent current density. We explain the differences between these tensors and conventional estimates of apparent resistivity and phase for simple resistivity environments and demonstrate, using canonical models in 1-D and 2-D environments, that both tensors are more sensitive to vertical and horizontal resistivity gradients than their conventional counterparts. The properties of the new tensors are explained using electromagnetic induction theory and the effects of associated charges at resistivity boundaries. We introduce a new way to plot tensor ellipses, which brings significant improvements to the interpretation of MT data, using appropriate visualization software. The apparent resistivity tensor gives information about the magnitude and direction of apparent resistivity subsurface structures and has a strong response to vertical resistivity contrasts. The resistivity phase tensor is highly sensitive to vertical boundaries and the associated fields in the TM mode. It is also free from static distortions under the same conditions implied for the conventional phase tensor. These findings have prompted a study in the potential of the new tensors for 3-D inversions. The results from a 3-D inversion of a canonical oblique conductor straddling two quarter spaces show distinct improvements in resolving the boundaries of the conductor and open a promising field for future studies.

1. Introduction

The period-dependent magnetotelluric (MT) response tensor ($\boldsymbol{Z}$) relates the horizontal electric and magnetic fields measured at the Earth's surface. It is the fundamental parameter in the MT method and is used to obtain information about the resistivity structure of the Earth. The MT response tensor is usually presented as period-dependent apparent resistivity ($\rho_{a,Z}$) and phase (φ) curves that are directly derived from tensor components as $\rho_{a,Zij} = (\mu/\omega)|Z_{ij}|^2$ and $\varphi_{ij} = tan^{-1}(Im(Z_{ij})/\ Re\ (Z_{ij}))$. This concept originates with the one-dimensional interpretation of subsurface resistivity structures (e.g., Vozoff, 1986) related to the off-diagonal elements of $\boldsymbol{Z}$ exclusively. The curves can be used to present MT data prior to inversion approaches and allow for some preliminary conclusions on the resistivity depth distribution if the diagonal tensor elements are close to zero. If the response is highly three-dimensional, the diagonal tensor elements will be significantly different from zero and the interpretation of the apparent resistivity and phase curves will be difficult and less intuitive.

The phase tensor (PT) introduced by Caldwell et al. (2004) reduces the MT response tensor to its phase information and provides the possibility to visualize the tensors by their principal components (maximum and minimum phases) and associated orientations. Methods for the presentation of tensors as ellipses have been presented by various authors (e.g., Bibby, 1986; Bibby et al., 2005; Booker, 2014; Caldwell et al., 2004; Caldwell & Bibby, 1998; Moorkamp, 2007), and they allow for a compact representation of spatial and period-dependent tensor information.

Several studies have introduced apparent resistivity tensors in different contexts: Caldwell and Bibby (1998) used them for long-offset time domain electric field data, Caldwell et al. (2002) used them to present controlled-source MT data, and Weckmann et al. (2003) showed examples for natural source field MT data. Brown (2016) developed the theory to define an extended-Born MT scattering tensor and apparent background electric and magnetic fields from a complex apparent conductivity tensor. In this paper we use the inverse of this apparent conductivity tensor, the complex apparent resistivity tensor, and decompose it into

a real and imaginary tensor. Here, the real tensor is directly comparable to the apparent resistivity tensor in Weckmann et al. (2003). In addition, we introduce the resistivity phase tensor, which is closely related to the imaginary part of the complex apparent resistivity tensor. It quantifies an additional *spatial dispersion* and is associated with the horizontal gradient of the resistivity in the region where most of the electric current is focused. The theoretical developments in Brown (2016) suggested that the new tensors could provide a useful, intuitive, and compact method for the presentation of all MT data, in a coordinate system independent of that chosen to measure the electromagnetic (EM) fields. Geophysical and geological interpretations in 3-D resistivity environments could be simplified if well-established graphical representations of the tensors as ellipses are deployed.

The primary purpose of this paper is to explore the effectiveness—and limitations—of the new tensors, to visualize MT data and provide insight to the underlying EM processes in multidimensional resistivity environments. The COMSOL Multiphysics® platform is used to generate EM fields from a suite of canonical, 1-D isotropic, 1-D anisotropic, and 2-D resistivity models. The electric, magnetic, and current density fields are exported to visualization software with the flexibility to display the fields and associated MT tensors in a variety of forms. The forward modeling studies revealed a high sensitivity of the new tensors to horizontal and vertical resistivity contrasts, which led us to investigate their potential to improve the resolution of resistivity anomalies in 3-D inversions. The results are compared to established inversion parameters, such as the complex impedance tensor (e.g., Heise et al., 2008; Kelbert et al., 2012; Meqbel et al., 2016; Tietze & Ritter, 2013) and exclusive phase tensor inversions (Patro et al., 2013; Tietze et al., 2015). A comprehensive review about these approaches that also addresses the resolvability of resistivity structures is given by Miensopust (2017).

The paper is organized into three subsequent sections. Section 2 introduces the concept of apparent resistivity and resistivity phase tensors, whose (real) elements can be compared easily with the conventional definitions of apparent resistivity and phase, and elements of the phase tensor (Caldwell et al., 2004) in 1-D and 2-D resistivity environments. Section 3 focuses on forward modeling studies using COMSOL Multiphysics®. First, the period-dependent changes and sensitivities of the new tensors to a simple 1-D resistivity structure are investigated in the context of EM induction (section 3.1). Section 3.2 shows an example of the MT tensors for a 1-D anisotropic layered-Earth resistivity model to demonstrate the period-dependent changes in the ellipse parameters representing some of the MT tensors. Section 3.3 presents the numerical modeling results of a 2-D isotropic resistivity plate model and describes the spatial and period-dependent behavior of the tensor ellipses associated with EM induction and charges at resistivity boundaries. In section 4 the new tensors are incorporated into the 3-D MT inversion software ModEM (Kelbert et al., 2014). Their performance is tested using a canonical 3-D model (Tietze et al., 2015), and the results are compared with those from the conventional MT response tensor ($\boldsymbol{Z}$) and phase tensor ($\boldsymbol{\phi}$).

2. The Apparent Resistivity Tensor and the Resistivity Phase Tensor

The relationship $\boldsymbol{E}_h = \boldsymbol{Z}\boldsymbol{B}_h$ between the horizontal electric field and magnetic induction, $\boldsymbol{E}_h$ (V/m) and $\boldsymbol{B}_h$ (T) respectively, at the surface of the Earth, contains information about the subsurface electrical conductivity in the period-dependent 2 by 2 MT response tensor, $\boldsymbol{Z}$ (m/s). Brown (2016) used an analogy for the propagation of plane EM waves through a homogeneous, dissipative, and anisotropic conductivity model half-space to construct a second rank 3 by 3 tensor $\boldsymbol{\gamma}$ (m^{-2}) consisting of quadratic functions of complex wave numbers associated with the EM waves in the model. The approach has similarities with the *c-response* (Schmucker, 1987), which relates a 1-D resistivity distribution to the first vertical derivative of the horizontal electric field. In the following, the formulations of Brown (2016) are restricted to the horizontal EM fields and all tensors ($\boldsymbol{Z}, \boldsymbol{\gamma}, \boldsymbol{\sigma}, \boldsymbol{\sigma}_a, \boldsymbol{\rho}_a$) have a dimension of 2 by 2.

In a uniform anisotropic half-space the complex wave numbers of $\boldsymbol{\gamma}$ reduce to vertical wave numbers and the electrical conductivity properties related to the second vertical derivative of the horizontal electric field are given by

$$\frac{\partial^2 \mathbf{E}_\mathrm{h}}{\partial z^2} = \boldsymbol{\gamma}\,\mathbf{E}_\mathrm{h} = (\mathrm{i}\omega\mu\boldsymbol{\sigma})\,\mathbf{E}_\mathrm{h} = \mathrm{i}\omega\mu\,\mathbf{J}_\mathrm{h} \tag{1a}$$

where $\boldsymbol{\sigma}$ is the actual horizontal anisotropic conductivity tensor and $\boldsymbol{J}_h$ is the actual (2 × 1) current density vector at an observation point.

For an arbitrary subsurface conductivity structure, the conductivity tensor and the current density vector become apparent quantities $\boldsymbol{\sigma}_a$ and $\boldsymbol{J}_a$, respectively, where $\boldsymbol{J}_a$ (A/m^2) is the (2 × 1) apparent current density vector required to satisfy the equality with the second vertical derivative of $\boldsymbol{E}_h$ at the observation point. In nonuniform environments (1a) becomes

$$\frac{\partial^2 \mathbf{E}_\mathrm{h}}{\partial z^2} = \boldsymbol{\gamma}_\mathrm{a}\,\mathbf{E}_\mathrm{h} = (\mathrm{i}\omega\mu\boldsymbol{\sigma}_\mathrm{a})\,\mathbf{E}_\mathrm{h} = \mathrm{i}\omega\mu\,\mathbf{J}_\mathrm{a} \tag{1b}$$

The concept of a complex apparent conductivity tensor $\boldsymbol{\sigma}_a$ (S/m) is similar to that of the apparent resistivity ($\rho_{a,Z}$) derived from the MT response tensor $\boldsymbol{Z}$ in nonuniform environments. For measurements at the surface above an arbitrary conductivity structure, it characterizes the electrical properties in a volume beneath the measurement site. Its real part represents the dissipative behavior of the subsurface, and its imaginary part represents the effects on the phases due to EM induction in the presence of conductivity variations with depth (1-D structures) and additional effects due to electric fields from charges associated with lateral conductivity heterogeneities (2-D and 3-D structures).

The apparent conductivity tensor is a quadratic function of $\boldsymbol{Z}$ given by (Brown, 2016)

$$\boldsymbol{\sigma}_\mathrm{a} = \left(\frac{-\mathrm{i}\omega}{\mu}\right)\det(\mathbf{Y})\,\mathbf{Z}^\mathrm{T}\,\mathbf{Y} \tag{2}$$

where μ is the free space magnetic permeability, det represents the determinant of a matrix, the superscript T represents the transpose, and $\boldsymbol{Y} = \boldsymbol{Z}^{-1}$ (s/m) is the inverse of the MT response tensor. The complex apparent resistivity tensor, $\boldsymbol{\rho}_a$ (Ω m), is therefore defined as

$$\boldsymbol{\rho}_a = \left(\frac{i\mu}{\omega}\right)\det(\boldsymbol{Z})\,\boldsymbol{Z}\,\boldsymbol{Y}^T \tag{3}$$

An apparent current density vector, $\boldsymbol{J}_a$, consistent with the definition in (1b), is related to the observed electric and magnetic fields at a point on the surface by

$$\boldsymbol{E}_h = \boldsymbol{\rho}_a\,\boldsymbol{J}_a = \left(\frac{i\mu}{\omega}\right)\det(\boldsymbol{Z})\,\boldsymbol{Z}\,\boldsymbol{Y}^T\,\boldsymbol{J}_a \tag{4a}$$

$$\boldsymbol{B}_h = \left(\frac{i\mu}{\omega}\right)\det(\boldsymbol{Z})\,\boldsymbol{Y}^T\,\boldsymbol{J}_a \tag{4b}$$

The complex apparent resistivity tensor in (3) can be regarded as a normalisation of the observed MT electric field with respect to an apparent current density related to the observed magnetic field in (4b).

The complex apparent resistivity tensor can be decomposed into real and imaginary parts, and magnitude and phase:

$$\boldsymbol{\rho}_\mathrm{a} = \mathbf{U}_\mathrm{a} + \mathrm{i}\mathbf{V}_\mathrm{a} = \mathbf{U}_\mathrm{a}\left(\mathbf{I} + \mathrm{i}\mathbf{U}_\mathrm{a}^{-1}\mathbf{V}_\mathrm{a}\right) = \mathbf{U}_\mathrm{a}\,(\mathbf{I} + \mathrm{i}\boldsymbol{\phi}_\mathrm{a}) \tag{5}$$

which provides new definitions of $\boldsymbol{U}_a$ and $\boldsymbol{\phi}_a$ as the apparent resistivity tensor and resistivity phase tensor, respectively. The components of $\boldsymbol{U}_a$, $\boldsymbol{V}_a$ and $\boldsymbol{\phi}_a$ can be derived as functions of the real and imaginary parts of the MT response tensor $\boldsymbol{Z}$, by expanding (3) with the definitions of the quantities in (5; see Appendix B).

To distinguish the new tensors from existing MT parameters, for example, the phase tensor (PT, $\boldsymbol{\phi}$), the acronyms CART, RT, and RPT are introduced for the complex apparent resistivity tensor ($\boldsymbol{\rho}_a$), apparent resistivity tensor ($\boldsymbol{U}_a$), and resistivity phase tensor ($\boldsymbol{\phi}_a$), respectively.

2.1. Distortion

Distortions of electric and magnetic fields at an observation site are the consequences of changes in regional electric currents caused by, for example, electrical coupling among regional structures (e.g., Park, 1985), local subsurface conductivity heterogeneities (e.g., Groom & Bailey, 1989), and topography (e.g., Jiracek, 1990). It is crucial to account for those effects during the visual interpretation and modeling/inversion of MT data. Thus, the following section examines the impact from distortion on the new MT tensors.

A rigorous treatment of EM distortion due to local structures (Chave & Smith, 1994) relates the horizontal components of the observed, distorted EM fields, $\boldsymbol{E}_h$ and $\boldsymbol{B}_h$ to their regional, undistorted counterparts, $\boldsymbol{E}_h^r$ and $\boldsymbol{B}_h^r$ by

$$\boldsymbol{E}_h = \boldsymbol{C}\boldsymbol{E}_h^r \tag{6a}$$

$$\boldsymbol{B}_h = \boldsymbol{B}_h^r + \boldsymbol{D}\boldsymbol{E}_h^r = (\boldsymbol{I} + \boldsymbol{D}\boldsymbol{Z}^r)\boldsymbol{B}_h^r \tag{6b}$$

where the superscript r refers to regional fields, and $\boldsymbol{C}$ and $\boldsymbol{D}$ are real, period-independent, second rank, 2×2 electric and magnetic distortion tensors, respectively. The distorted MT response tensor $\boldsymbol{Z}$ is

$$\mathbf{E}_\mathrm{h} = \mathbf{C}\mathbf{Z}^\mathrm{r}(\mathbf{I} + \mathbf{D}\mathbf{Z}^\mathbf{r})^{-1}\mathbf{B}_\mathrm{h} = \mathbf{Z}\mathbf{B}_\mathrm{h} \tag{6c}$$

The original phase tensor analysis (Bibby et al., 2005; Caldwell et al., 2004) makes the common assumption of static (galvanic) distortion where the condition $\boldsymbol{D} = 0$ implies that $\boldsymbol{B}_h = \boldsymbol{B}_h^r$ and $\boldsymbol{Z} = \boldsymbol{C}\boldsymbol{Z}^\boldsymbol{r}$. This results in an observed electric field that is a linear superposition of the regional field and a scattered electric field in-phase with the regional field. The PT is defined by decomposing $\boldsymbol{Z}$ into its real and imaginary parts, $\boldsymbol{U}$ and $\boldsymbol{V}$ respectively, so that $\boldsymbol{Z} = (\boldsymbol{U} + i\boldsymbol{V}) = \boldsymbol{U}(\boldsymbol{I} + i\boldsymbol{\phi})$ and, similarly, $\boldsymbol{Z}^r = \boldsymbol{U}^r(\boldsymbol{I} + i\boldsymbol{\phi}^r)$. From this it is easily verified that $\boldsymbol{\phi} = \boldsymbol{\phi}^r$ and therefore the PT $\boldsymbol{\phi}$ is distortion-free. The inverse of the MT response tensor $\boldsymbol{Y}$, its transpose $\boldsymbol{Y}^T$, and their associated phase tensors $\boldsymbol{\phi}_Y$ and $\boldsymbol{\phi}_Y^T$ respectively, are given by

$$\mathbf{Y} = \mathbf{U}_\mathrm{Y} + \mathrm{i}\mathbf{V}_\mathrm{Y} = (\mathbf{I} + \mathrm{i}\boldsymbol{\phi}_\mathrm{Y})\,\mathbf{U}_\mathrm{Y} \tag{7a}$$

$$\boldsymbol{\phi}_\mathrm{Y} = \mathbf{V}_\mathrm{Y}\mathbf{U}_\mathrm{Y}^{-1} = -\boldsymbol{\phi} \tag{7b}$$

$$\boldsymbol{\phi}_\mathrm{Y}^\mathrm{T} = -\boldsymbol{\phi}^\mathrm{T} \tag{7c}$$

As Booker (2014) noted, the phase tensor is purely a property of the observed MT response tensor, its geometry is independent of the assumption that $\boldsymbol{B}_h = \boldsymbol{B}_h^r$ so it is meaningful even if the horizontal magnetic field is distorted.

If $\boldsymbol{D} = 0$, (6b) and (4b) imply that the apparent current density $\boldsymbol{J}_a = \boldsymbol{J}_a^r$ is distortion-free, consistent with the condition $\boldsymbol{B}_h = \boldsymbol{B}_h^r$. From (6a) and (4a), the distorted electric field is therefore

$$\mathbf{E}_\mathrm{h} = \mathbf{C}\mathbf{E}_\mathrm{h}^\mathrm{r} = \mathbf{C}\left(\boldsymbol{\rho}_\mathrm{a}^\mathrm{r}\mathbf{J}_\mathrm{a}^\mathrm{r}\right) = \left(\mathbf{C}\boldsymbol{\rho}_\mathrm{a}^\mathbf{r}\right)\mathbf{J}_\mathrm{a}^\mathrm{r} \tag{8a}$$

Therefore, the relationship between the distorted apparent resistivity tensor and the regional resistivity tensor is

$$\boldsymbol{\rho}_\mathrm{a} = \mathbf{C}\boldsymbol{\rho}_\mathrm{a}^\mathrm{r} \tag{8b}$$

From the definition of $\boldsymbol{\phi}_a$ in (5), and following the approach in Caldwell et al. (2004):

$$\boldsymbol{\phi}_\mathrm{a} = \mathbf{U}_\mathrm{a}^{-1}\mathbf{V}_\mathrm{a} = \left(\mathbf{C}\mathbf{U}_\mathrm{a}^\mathrm{r}\right)^{-1}\left(\mathbf{C}\mathbf{V}_\mathrm{a}^\mathrm{r}\right) = \left(\mathbf{U}_\mathrm{a}^\mathrm{r}\right)^{-1}\mathbf{V}_\mathrm{a}^\mathrm{r} = \boldsymbol{\phi}_\mathrm{a}^\mathrm{r} \tag{8c}$$

where $\boldsymbol{U}_a^r$ is the (undistorted) regional RT. Hence, the RT ($\boldsymbol{U}_a$) is distorted and the RPT ($\boldsymbol{\phi}_a$) is free from distortion if the condition $\boldsymbol{D} = 0$ is imposed.

If local conductive heterogeneities are very different from regional structures, the condition $\boldsymbol{J}_a = \boldsymbol{J}_a^r$ may not be a good approximation so the regional horizontal magnetic field may be changed. Brown (2016, equation 28) assumed that similar to the electric field, the distorted magnetic field is also a linear superposition of the regional magnetic field and a scattered magnetic field in-phase with the regional magnetic field. In these circumstances, a single 2×2 tensor $\boldsymbol{C}$ is sufficient to parameterize the distortion of both EM fields. The distorted apparent current density and distorted magnetic field are related using (4)

$$\mathbf{B}_\mathrm{h} = \left(\frac{\mathrm{i}\mu}{\omega}\,\det(\mathbf{Z})\mathbf{Y}^\mathrm{T}\right)\mathbf{J}_\mathrm{a} \tag{9a}$$

$$= \left(\frac{\mathrm{i}\mu}{\omega}\,\det(\mathbf{C})\det(\mathbf{Z}^\mathrm{r})\left(\mathbf{C}^{-1}\right)^\mathrm{T}(\mathbf{Y}^\mathrm{r})^\mathrm{T}\right)\mathbf{J}_\mathrm{a} \tag{9b}$$

$$= \left(\frac{\mathrm{i}\mu}{\omega}\,\det(\mathbf{Z}^\mathrm{r})(\mathbf{Y}^\mathrm{r})^\mathrm{T}\right)\mathbf{P}^{-1}\mathbf{J}_\mathrm{a} \tag{9c}$$

where the tensor $\boldsymbol{P}^{-1} = (\det(\boldsymbol{C}))^{-1}(\boldsymbol{Z}^r)^T\boldsymbol{C}^T(\boldsymbol{Y}^r)^T$ and $\boldsymbol{P}^{-1}\boldsymbol{J}_a = g\boldsymbol{J}_a^r$ where g is a real scalar, equal to unity if $\boldsymbol{C}$ is known independently. The tensor $\boldsymbol{P}$ is complex, so the amplitude and phase of the distorted apparent current density must be different from the regional apparent current density for a distorted magnetic field assumed to be in-phase with the regional magnetic field. From (9b), the observed electric field in this model is

$$\mathbf{E}_{\mathrm{h}} = \mathbf{Z}\mathbf{B}_{\mathrm{h}} = \det(\mathbf{C})\,\mathbf{C}\left(\frac{\mathrm{i}\mu}{\omega}\,\det(\mathbf{Z}^{\mathrm{r}})\mathbf{Z}^{\mathrm{r}}\left(\mathbf{C}^{-1}\right)^{\mathrm{T}}(\mathbf{Y}^{\mathrm{r}})^{\mathrm{T}}\right)\mathbf{J}_{\mathrm{a}} = \boldsymbol{\rho}_{\mathrm{a}}^{\mathrm{m}}\mathbf{J}_{\mathrm{a}} \tag{10}$$

where $\boldsymbol{\rho}_a^m$, the CART in the presence of distorted electric and magnetic fields, which are in-phase with their respective regional fields, can be decomposed into real and imaginary parts, $\boldsymbol{U}_a^m$ and $\boldsymbol{V}_a^m$ respectively. It is easily verified (numerically) that the RPT $\boldsymbol{\phi}_a^m = \left(\boldsymbol{U}_a^m\right)^{-1}\boldsymbol{V}_a^m = \boldsymbol{\phi}_a^r$, so it is distortion-free. As the PT $\boldsymbol{\phi}$ is also distortion-free in this model (Brown, 2016), the RPT $\boldsymbol{\phi}_a$, defined in (5), is free from distortion under the same conditions imposed for the conventional PT. If local heterogeneities are so strong that the distorted and regional magnetic fields are not in phase, Brown (2016, equation 30) may be employed.

The findings above imply that similar to the PT, the RPT is a suitable interpretation and/or inversion parameter in the presence of galvanic distortion.

2.2. Comparison of Different Definitions

The matrix elements of $\boldsymbol{U}_a$ may be compared simply with the conventional definition, $\rho_{a,Zij} = (\mu/\omega)|Z_{ij}|^2$ for resistivity distributions based upon MT response tensors with off-diagonal elements only (uniform half-spaces, 1-D isotropic, 1-D horizontally anisotropic, and 2-D distributions in a coordinate system aligned with the strike). In terms of U_{ij},V_{ij}, the real and imaginary parts of Z_{ij}, respectively, these are

$$\mathbf{U}_{\mathrm{a}} = \frac{\mu}{\omega}\begin{pmatrix} 2\mathrm{U}_{12}\mathrm{V}_{12} & 0 \\ 0 & 2\mathrm{U}_{21}\mathrm{V}_{21} \end{pmatrix} \tag{11a}$$

$$\rho_{\mathrm{a,Zij}} = \frac{\mu}{\omega}\left(\mathrm{U}_{\mathrm{ij}}^2 + \mathrm{V}_{\mathrm{ij}}^2\right) \tag{11b}$$

The elements of the RT are different from $\rho_{a,Zij}$, except where $U_{ij} = V_{ij}$ at sites above a uniform half-space or horizontally anisotropic half-space in strike coordinates.

The RPT quantifying the phase differences between the horizontal electric and apparent current density fields does not have a simple relationship with the PT or the conventional phase of the MT response tensor, $\varphi_{ij} = \tan^{-1}(V_{ij}/U_{ij})$, because the latter two represent the phase differences between the electric and magnetic fields. In the absence of any distortion, the relationship between the RPT and the PT is

$$\begin{aligned}\boldsymbol{\phi}_a = {} & \left(\mathrm{tr}(\boldsymbol{\phi})\left(\boldsymbol{U}_Y^T + \boldsymbol{\phi}\boldsymbol{U}_Y^T\boldsymbol{\phi}^T\right) + \left(\det(\boldsymbol{\phi}) - 1\right)\left(\boldsymbol{U}_Y^T\boldsymbol{\phi}^T - \boldsymbol{\phi}\boldsymbol{U}_Y^T\right)\right)^{-1} \\ & \times\left(-\mathrm{tr}(\boldsymbol{\phi})\left(\boldsymbol{U}_Y^T\boldsymbol{\phi}^T - \boldsymbol{\phi}\boldsymbol{U}_Y^T\right) + \left(\det(\boldsymbol{\phi}) - 1\right)\left(\boldsymbol{U}_{Yh}^T + \boldsymbol{\phi}\boldsymbol{U}_Y^T\boldsymbol{\phi}^T\right)\right)\end{aligned} \tag{12}$$

where *tr* is the trace of a matrix.

For the class of resistivity distributions based upon MT response tensors with off-diagonal elements only, (12) simplifies to a relationship between $\boldsymbol{\phi}_a$ and $\boldsymbol{\phi}$ where both quantities are distortion-free:

$$\boldsymbol{\phi}_a = 0.5\left(\mathrm{tr}\left(\boldsymbol{\phi} - \boldsymbol{\phi}^{-1}\right)\boldsymbol{I} - \left(\boldsymbol{\phi} - \boldsymbol{\phi}^{-1}\right)\right) \tag{13}$$

It is instructive to compare the matrix elements of $\boldsymbol{\phi}_a$ and $\boldsymbol{\phi}$ for this class:

$$\boldsymbol{\phi}_{\mathrm{a}} = \begin{pmatrix} \dfrac{\left(\mathrm{V}_{12}^2 - \mathrm{U}_{12}^2\right)}{2\mathrm{V}_{12}\mathrm{U}_{12}} & 0 \\ 0 & \dfrac{\left(\mathrm{V}_{21}^2 - \mathrm{U}_{21}^2\right)}{2\mathrm{V}_{21}\mathrm{U}_{21}} \end{pmatrix} \tag{14a}$$

$$\boldsymbol{\phi} = \begin{pmatrix} \dfrac{\mathrm{V}_{21}}{\mathrm{U}_{21}} & 0 \\ 0 & \dfrac{\mathrm{V}_{12}}{\mathrm{U}_{12}} \end{pmatrix} \tag{14b}$$

The (arctangents of the) diagonal elements of the PT have the same magnitude as the conventional phase of the MT response tensor φ_{ij}. The RPT elements are, however, composed of quadratic differences rather than linear ratios in the PT elements. As will be shown in the next section, this implies that the RPT is more sensitive to the structure of 1-D isotropic (and anisotropic) media than the PT.

2.3. Ellipse Parameters

In this section the calculation and representation of the tensor ellipse principal axes is addressed. We demonstrate for the first time how to visualize and understand the fundamental physics behind the new tensors.

An arbitrary 2×2 second rank tensor $\boldsymbol{\chi}$ can be represented as an ellipse in the x-y plane defined by four parameters that are constructed from the four tensor elements. Three of these parameters are invariant to a rotation about the z axis; these are the magnitudes of the principal major and minor axes of the ellipse $\chi_{\max}$ and $\chi_{\min}$, respectively, and a skew angle β, which defines the position of the major axis relative to a reference axis. In the case of the CART, the angle δ between the major axes of $\boldsymbol{U}_a$ and $\boldsymbol{V}_a$ represents an additional invariant. The fourth parameter is the angle α, which defines the position of the reference axis relative to the coordinate axes. In this study all angles are counterclockwise from the coordinate axis pointing eastward.

The calculation of the ellipse parameters (e.g., Bibby et al., 2005; Caldwell et al., 2004; Moorkamp, 2007) corresponds to a singular value decomposition where the singular values represent the principal ellipse axes magnitudes. However, singular value decompositions are nonunique, and the calculation of the ellipse axis direction and the determination of the correct quadrant of the principal values can pose a problem if one or both of the principal axes becomes negative (Booker, 2014). As will be shown in the next sections this applies for the RPT and it is also true for the imaginary part of the CART. Booker (2014) includes the circulation direction of a tensor to obtain unambiguous measures for the principal signs and axes directions. We therefore adapt his method and compute the ellipse parameters using the equations in Appendix A.

The common presentation of the tensors as ellipses hampers the recognition of the size of the principal axes. To address this problem, the ellipses are often normalized and color coded by the value of the major axis with the result that the size of the minor axis can be difficult to read. Häuserer and Junge (2011) plot the major and minor axes as colored orthogonal bars, but in uniform or 1-D situations the orientation of the bars is arbitrary and confusing. For this reason, we introduce a combination of both schemes and plot the ellipses color coded by the value of the major axis and superpose the minor axis as a bar with its respective color. Thus, the orientation of the principal axes will only become relevant in higher dimensional (or anisotropic 1-D) environments.

For the CART ($\boldsymbol{U}_a$ and $\boldsymbol{V}_a$) the size of the minor axis is relative to the size of the major axis by a logarithmic scale, whereas the length of the major axis is kept constant. As the principal axes of $\boldsymbol{V}_a$ may become negative, the length of the axes reflect absolute values, while the linear color range includes negative resistivity values. For the RPT and the PT the sizes of the ellipses/bars are proportional to the arctangents of the principal axes. To account for negative values for $\boldsymbol{\phi}_a$ the size of the axes equals the absolute value and the color range is extended from $-90°$ to $90°$ ($0°$ to $90°$ for the PT). Note that in this plotting scheme the major axes will always correspond to the largest absolute (positive or negative) tensor axis. Similar to $\boldsymbol{U}_a$ and $\boldsymbol{V}_a$, each ellipse principal axis of the phase tensors is normalized by its corresponding major axis. To prevent vanishing ellipses for principal values close (or equal) to zero, absolute values of $2°$ (or 2 Ωm for $\boldsymbol{V}_a$) were added to the minor and major axes of each tensor (not affecting the color values).

In Figure 1 the tensor ellipses are plotted for a 1-D layered resistivity model (Figure 1a), a 2-D resistivity distribution consisting of two quarter spaces (Figure 1b), and an arbitrary 3-D structure (Figure 1c). The model in Figure 1a comprises a 2-km-thick conductive layer at 2-km depth. For 1-D models the major and minor axes of the MT tensors have equal magnitudes and their representation corresponds to a uniform circle. The circles in Figure 1a refer to a period of 100 s, which is representative for EM fields that pass from the conductive layer to the underlying resistive half-space. In such case the principal axes of $\boldsymbol{V}_a$ and $\boldsymbol{\phi}_a$ become negative and those of $\boldsymbol{\phi}$ are smaller than $45°$. For the interpretation of the 2-D ellipses in Figure 1b it is emphasized that the CART and its derivatives RT, RPT, and $\boldsymbol{V}_a$ are driven by changes in the electric fields, while the PT is driven by the magnetic field. This implies that $\boldsymbol{U}_a$, $\boldsymbol{V}_a$, and $\boldsymbol{\phi}_a$ axes perpendicular to the strike (currents crossing the boundary) refer to the TM mode and axes parallel to the boundary refer to the TE mode and vice versa for the PT. The individual modes are represented by the minor or the major

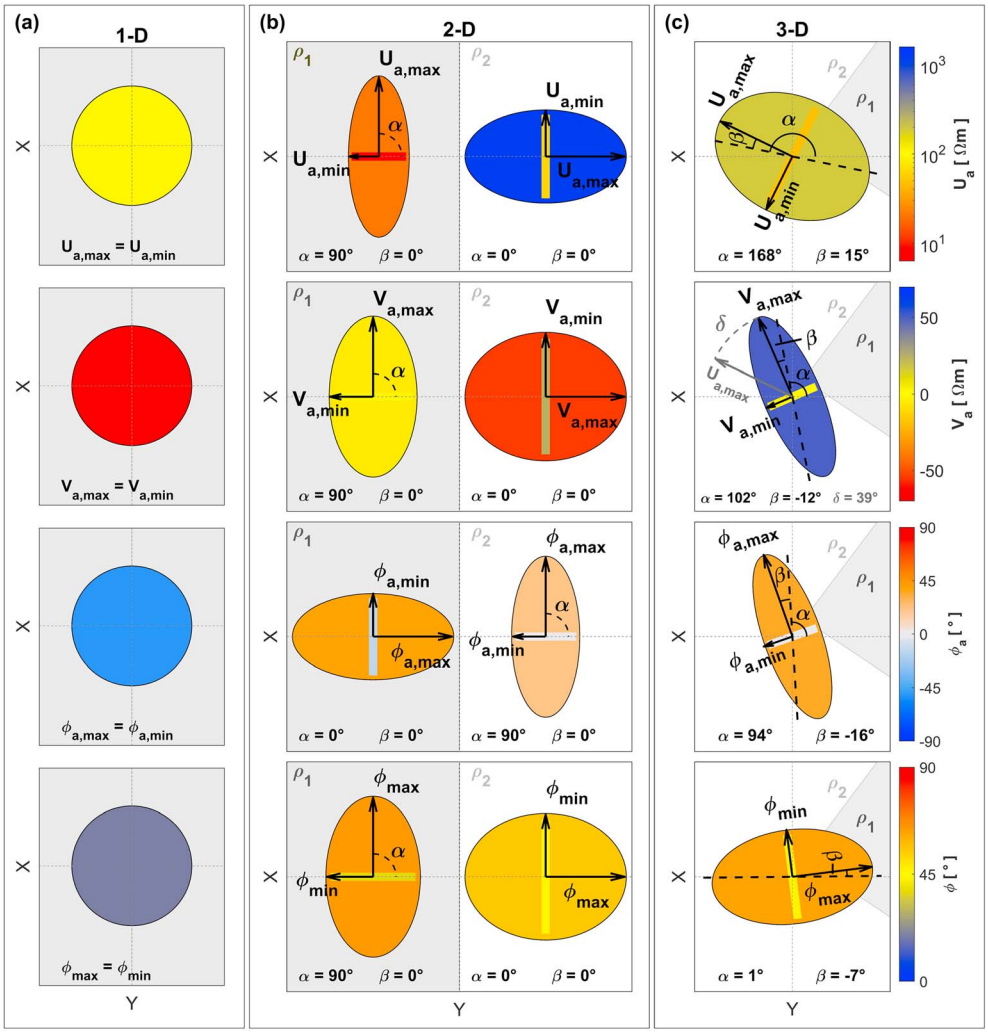

Figure 1. The geometrical representation of tensors as ellipses for a 1-D, 2-D, and 3-D resistivity distribution. (a) $\boldsymbol{U}_a$, $\boldsymbol{V}_a$, $\boldsymbol{\phi}_a$, and $\boldsymbol{\phi}$ ellipses (top to bottom) above a 1-D resistivity distribution (2-km-thick conductive layer with 10 Ω m resistivity at 2-km depth; background resistivity: 1,000 Ω m). The tensors are shown for a target period of 100 s, representative for EM fields leaving the conductive layer and entering the resistive half-space. This results in negative $\boldsymbol{V}_a$ and $\boldsymbol{\phi}_a$ principal axes. (b) $\boldsymbol{U}_a$, $\boldsymbol{V}_a$, $\boldsymbol{\phi}_a$, and $\boldsymbol{\phi}$ ellipses at observation points on the conductive (left, $\rho_1 = 10$ Ω m) and resistive (right, $\rho_2 = 1{,}000$ Ω m) side of a 2-D resistivity distribution consisting of two quarter spaces with EM field measurement axes aligned to the direction of strike. The tensors are shown in 1.5-km distance to the boundary for a period of 10 s. Note how the orientations of the principal axes change across the boundary for each ellipse. (c) $\boldsymbol{U}_a$, $\boldsymbol{V}_a$, $\boldsymbol{\phi}_a$, and $\boldsymbol{\phi}$ ellipses at an observation point above a 3-D resistivity distribution (background $\rho_2 = 1{,}000$ Ω m, conductive anomaly $\rho_1 = 5$ Ω m at 2-km depth). The tensors are shown for a period of 5 s. Note the existence of finite invariant skew angles, β for each of the three ellipses and the finite mixed invariant angle, δ between $\boldsymbol{U}_a$ and $\boldsymbol{V}_a$ (shown in the $\boldsymbol{V}_a$ plot). The color values of the tensors in (a and b) correspond to the respective color bars in (c).

axis depending on the location of the site relative to the boundary (on the resistive or conductive side, cf. Figure 1b). $\boldsymbol{V}_a$ is generally sensitive to changes in the subsurface resistivity and does not represent any absolute resistivity values. If there is no change in resistivity, $\boldsymbol{V}_a$ is equal to zero. The RPT is directly related to $\boldsymbol{V}_a$, and parallel axes have always identical signs. For the 2-D situation in Figure 1b, the PT major and minor axes are orthogonal to the axes of the RPT. This changes when the major axes of the RPT become negative (cf. following sections). In that case the respective axes of the PT are smaller than 45° and are reflected by its minor axes. In 3-D environments the principal axes of $\boldsymbol{U}_a$, $\boldsymbol{V}_a$, $\boldsymbol{\phi}_a$, and $\boldsymbol{\phi}$ are not necessarily parallel. Here, the skew (β) of $\boldsymbol{U}_a$, $\boldsymbol{V}_a$, and $\boldsymbol{\phi}_a$ is generally more distinct than that of $\boldsymbol{\phi}$. As the RPT and the PT are free from galvanic distortion, an oblique orientation between the principal axes of both tensors is a clear indicator for three-dimensionality.

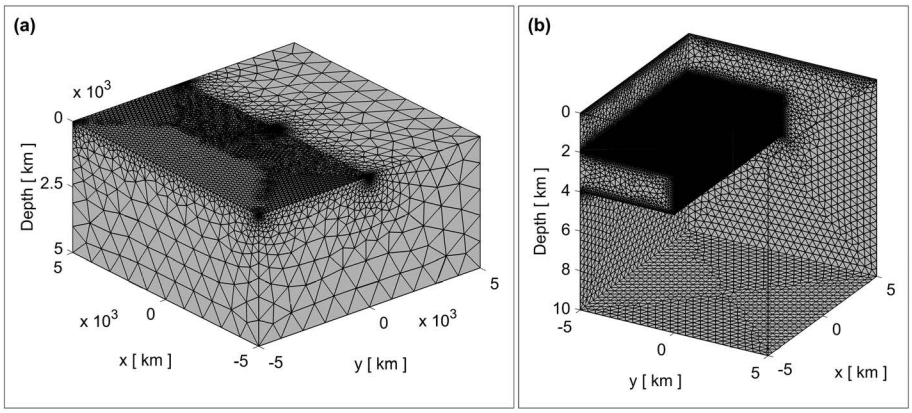

Figure 2. COMSOL finite element mesh for the 2-D plate model in section 3.3. The mesh elements are only visualized at selected object surfaces. (a) The dimension of the total model is 10,000 km × 10,000 km × 5,000 km and a 500-km air layer (not shown). The mesh elements in the outer box are coarse and become finer in the negative *y* direction to resolve the plate at 2-km depth. (b) The dimension of the inner model is 10 km × 10 km × 10 km. Here the mesh is very fine, especially to the surface and at the plate boundaries.

3. MT Tensors in Multidimensional Resistivity Environments

The fields and responses for the forward models shown in this section are calculated using COMSOL Multiphysics® 5.3. Detailed information about forward modeling using COMSOL is given in Löwer (2014), and examples of its application are shown in González-Castillo et al. (2015), Löwer and Junge (2017), and Cembrowski and Junge (2018). Generally, where the area of interest is restricted to the EM fields at the Earth's surface, a reasonable discretization accuracy of the model structures depends on the skin depth (δ_{max}), the target period, and site locations. For the studies shown here, the EM fields at depth were of equal interest, and therefore, the model discretization was chosen to be independent of the target frequency and included a very high resolution at geometric boundaries. All models (1-D and 2-D) were calculated in a three-dimensional environment with a total model expansion of $6\delta_{max} \times 6\delta_{max} \times 3\delta_{max}$ (x, y, z). To limit computational costs, an inner model grid (10 km × 10 km × 10 km) embracing all relevant geometries was defined (Figure 2). The need for a highly resolved inner grid resulted in up to 10^6 FE cells with more than 10^7 degrees of freedom. The EM wave equations were solved in the frequency domain for three/four periods per decade, using an iterative solver (BiCGStab, Biconjugate gradient stabilized) in combination with a multigrid algorithm. Using a multicore desktop system (8 cores at 3.4 GHz) with 64-GB internal memory, the run time for the plate model in section 3.3 (22 target periods) was ~3 hr. The fields and response functions shown in the following sections were extracted from the inner model via the COMSOL Multiphysics® 5.3 with MATLAB Livelink and visualized in MATLAB 2018a.

To validate the COMSOL modeling, analytical solutions of the MT response tensors have been computed using the horizontally anisotropic 1-D forward model of Dekker and Hastie (1980) and the general anisotropic 1-D forward model of Pek and Santos (2002). The 1-D isotropic and anisotropic models resulted in insignificant differences among the surface MT response tensors in all three methods. A comparison between the COMSOL and the Dekker and Hastie response for the anisotropic model in section 3.2 is given in the supporting information (Figure S1).

3.1. MT Tensors in 1-D Isotropic Environments

The assertions from section 2.2 are tested by investigating the period-dependent relationships among the diagonal elements of the RT, RPT, and PT and the conventional apparent resistivity ($\rho_{a,Z}$) for a 1-D isotropic model consisting of three layers with resistivity 1,000, 10, and 1,000 Ω m, thicknesses of 2,000 m for periods between 0.001 and 10,000 s (Figures 3a and 3b). For the phase tensors (RPT and PT) the arctangents of the diagonal elements are plotted. In addition to the diagonal elements, all tensors (RT, RPT, and PT) are visualized as ellipses for eight representative target periods. To illustrate the behavior of the EM fields, the magnitudes of the electric and magnetic fields and the current density are shown for two periods of 0.018 and 10 s (Figure 3c).

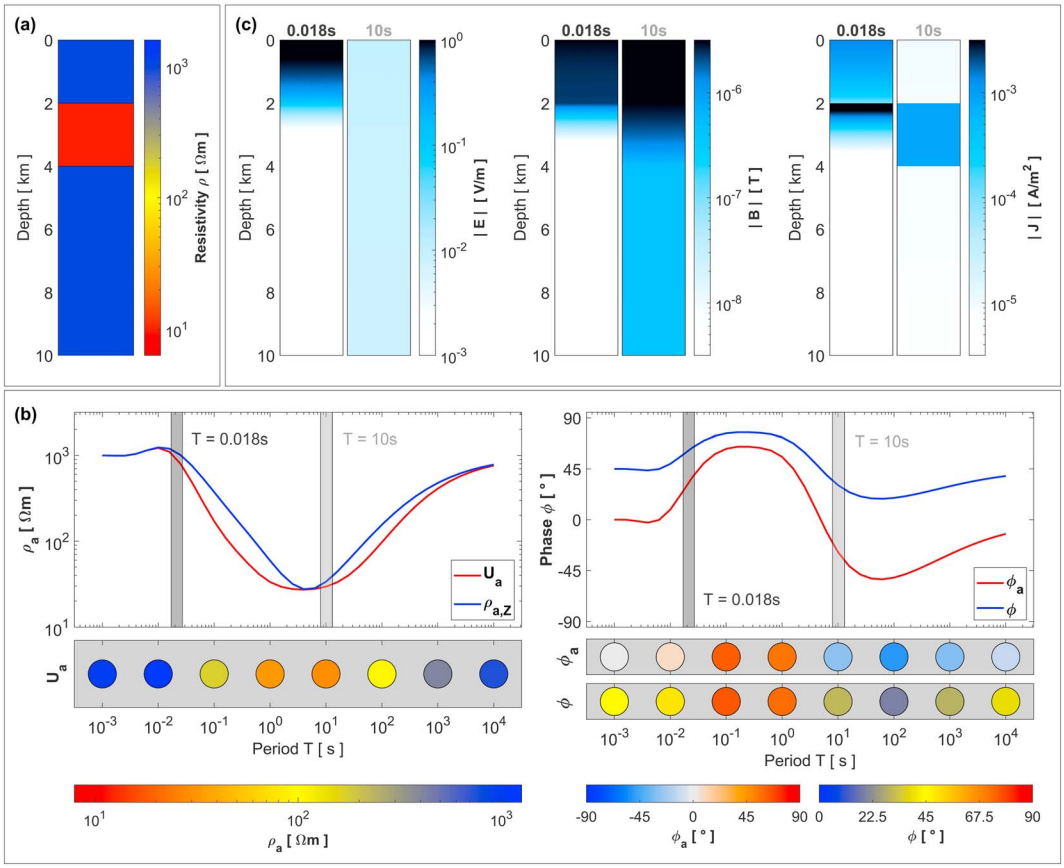

Figure 3. Results from a 1-D forward model. (a) The model comprises a conductor with a resistivity of 10 Ω m embedded in a 1,000 Ω m half-space. (b) Left: Apparent resistivity curves from the RT ($\boldsymbol{U}_a$) and the conventional apparent resistivity ($\rho_{a,Z}$) from the MT response tensor ($\boldsymbol{Z}$). $\boldsymbol{U}_a$ is additionally visualized by tensor ellipses for eight representative target periods. Right: Phase curves and tensor ellipses derived as the arctangents of the RPT ($\boldsymbol{\phi}_a$) and the conventional PT ($\boldsymbol{\phi}$). (c) The magnitudes of the electric field ($|\boldsymbol{E}|$), magnetic field ($|\boldsymbol{B}|$), and current density ($|\boldsymbol{J}|$) as depth sections for two periods (0.018 s (55.5 Hz) and 10 s).

In each layer (j = 1,3), the electric and magnetic fields behave (e.g., Kaufman & Keller, 1981) as

$$E^j = a_j e^{ik_j z} + b_j e^{-ik_j z}; B^j = {}^{k_j}/_{\omega}\left(a_j e^{ik_j z} - b_j e^{-ik_j z}\right); b_3 = 0; k_j = \sqrt{i\omega\mu_0\sigma_j}$$

For periods <0.003 s, the current density is in-phase with the electric field and both lead the magnetic field by 45° so the system is behaving like a uniform half-space. In Figure 3b this implies a constant apparent resistivity (U_a and $\rho_{a,Z}$) of 1,000 Ω m, a RPT of 0°, and a PT of 45°. For this period range the electric and magnetic field amplitudes decrease with depth in an oscillatory manner. The induced currents also decrease to zero with depth; in the upper part of the layer they give rise to a magnetic field that almost completely cancels the primary magnetic field beneath them and almost equals the primary magnetic field above them (Kaufman & Keller, 1981).

Between 0.003 and 0.3 s, the phase differences, between the magnetic field and its associated conduction currents, and the electric field, increase to a maximum due to the increase of the magnetic field associated with higher current density, particularly in the upper part of the second layer where the current density increases discontinuously across the first/second layer boundary (Figure 3c, fields at 0.018 s). At the surface, the magnetic field remains at twice the primary magnetic field amplitude, while the amplitude of the electric field slowly decreases, so decreasing the apparent resistivity. Simultaneously, RPT and PT increase to a maximum.

As the period increases (0.3–3 s), RPT and PT return to 0° and 45°, respectively. At the same time, the apparent resistivities reach a minimum.

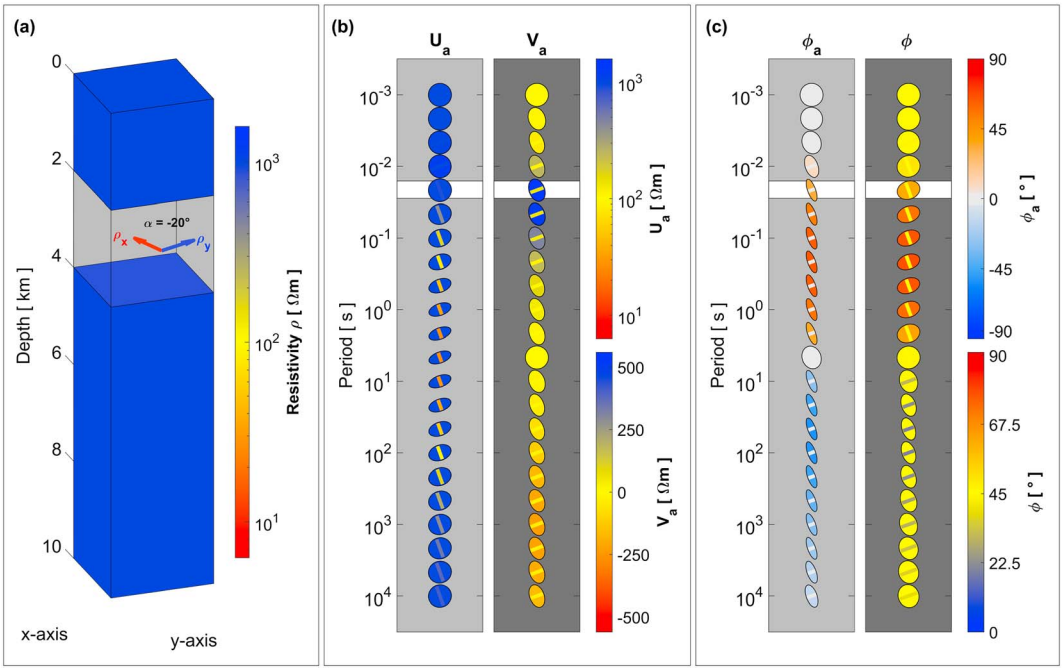

Figure 4. Results from a 1-D anisotropic forward model. (a) The resistivity model. (b) Period dependence of the RT ($\boldsymbol{U}_a$) and the imaginary part of the CART ($\boldsymbol{V}_a$). For periods >0.05 s, both tensors show the direction of the anisotropy. The RT exclusively presents apparent resistivity values. (c) RPT ($\boldsymbol{\phi}_a$) and conventional PT ($\boldsymbol{\phi}$). For periods from 0.05 to 5 s (sensitive to the anisotropic body) the minor and major axes have opposite directions. The highlighted period (0.021 s) is related to the fields shown in Figure 5.

For periods beyond 3 s, the RPT and the PT decrease to a minimum before returning to their uniform half-space values at the longest periods (>10,000 s). The apparent resistivity increases to the background value of 1,000 Ω m. At these periods, the magnetic field tends to decrease linearly with depth in the lowest third layer, while the decrease in the electric field is small. The currents are concentrated within the conductive anomaly (Figure 3c, fields at 10 s).

Figure 3b shows that the RT responds more rapidly than $\rho_{a,Z}$ with increasing period to the presence of the conductor, stays at a minimum for a wider period range, and emerges more steeply to reach the asymptotic value. This implies a higher sensitivity to resistivity contrasts in the vertical direction and might include the possibility of better resolution of thin conductive layers. The same applies to the RPT, which shows steeper gradients and higher variations in amplitude (by a factor of 2) compared to the conventional PT. It is emphasized that the half-space value of the RPT is at 0° (compared to 45° for the PT). This implies negative phase values for a transition from a conductor to a resistor.

The electric, magnetic, and current density field phases related to the model in Figure 3a are presented in Figure S2 (supporting information). In Figure S3 response curves and field amplitudes are shown for a 1-D model comprising a thin conductive layer of 200 m. They corroborate the improved resolution of a thin conductive layer using the new tensors.

3.2. MT Tensors in 1-D Anisotropic Environments

In this section we focus on the sensitivity of $\boldsymbol{U}_a$, $\boldsymbol{V}_a$, and $\boldsymbol{\phi}_a$ to a 1-D anisotropic resistivity distribution in comparison to the conventional phase tensor $\boldsymbol{\phi}$. A detailed discussion about the interpretation of the PT is given by Booker (2014), and the impact of electrical anisotropy on the MT response is summarized by Martí (2014).

The results from a 1-D anisotropic forward model are presented in Figure 4. The model comprises a 2-km-thick anisotropic layer whose top is at 2-km depth, embedded in a half-space with resistivity of 1,000 Ω m (Figure 4a). The anisotropic resistivities are 10 Ω m in the x direction (ρ_x) and 1,000 Ω m in the y direction

(ρ_y), rotated by −20° (i.e., counterclockwise). The coordinate system uses the MT convention with the x axis pointing north and the y axis pointing east.

In Figure 4b the tensors $\boldsymbol{U}_a$ and $\boldsymbol{V}_a$ are shown, representing the CART for a period range from 0.001 to 10,000 s. At the short periods (0.001–0.01 s), the major and minor axes of $\boldsymbol{U}_a$ have equal length consistent with the uniform background resistivity of 1,000 Ω m. With increasing period (>0.05 s) $\boldsymbol{U}_a$ responds to the anisotropic layer. The tensors are rotated by −20° to be aligned with the anisotropy directions, and the major axes are parallel to ρ_y and reproduce the resistivity value of 1,000 Ω m over the entire period range. The minor axes are parallel to ρ_x and show the transition from the overlying resistor into the conducting direction of the anisotropic body by decreasing apparent resistivity values. These reach a minimum at about 5 s and increase again with longer periods due to the underlying resistive half-space. The $\boldsymbol{V}_a$ tensors also demonstrate the anisotropy direction with their major axes parallel to the conducting anisotropy axis. In contrast to $\boldsymbol{U}_a$, the values of $\boldsymbol{V}_a$ respond to spatial changes (gradients) of the resistivity. Consequently, its response is largest when entering (positive values) and leaving (negative values) the anisotropic layer. In between the values go back to 0 Ω m (at ~5 s) representative of a uniform half-space. The minor axes are parallel to the resistive anisotropy direction, which equals the background resistivity. They are equal to 0 Ω m over the whole period range.

The RPT is related to the imaginary part of the CART so also responds to changes in the resistivity (Figure 4c). For the shortest periods, $\boldsymbol{\phi}_a$ and $\boldsymbol{\phi}$ take values of 0° and 45°, respectively, in a uniform half-space. With increasing period they are affected by the anisotropic body, showing a similar pattern as the isotropic case in section 3.1. The phases respond to the resistivity contrast at shorter periods than $\boldsymbol{U}_a$ (0.021 s), but just for the fields related to currents in the conductive directions. This causes the split and the alignment of the tensors with the anisotropy axes for the periods up to 5 s, where the minor and major axes of $\boldsymbol{\phi}$ and $\boldsymbol{\phi}_a$ have opposite directions. For longer periods, the lower boundary of the conductive layer produces PT values below 45° and RPT values below 0°. The tensor responses are reflected in the minor axes of the PT and the major axes of the RPT. For all periods the sensitive axis of the RPT is parallel to the conductive anisotropy direction and it is perpendicular in the case of the PT. The insensitive axes are 0° and 45°, respectively.

The magnitude and phase for the electric, magnetic, and current density fields related to the anisotropic 1-D model are shown (Figure 5) for a period of 0.021 s. In a generally anisotropic layer, the fields can be regarded as two independent pairs of downgoing and upgoing waves (Pek & Santos, 2002) so the fields may be visualized as two perpendicular depth slices, related to the magnetic field excitation in the x and y directions. Depending on the excitation, the magnetic and electric field components decrease either smoothly with depth (B_x excitation) or show abrupt changes (B_y excitation). Due to the oblique angle (−20° from the x axis) of the resistivity principal axes within the anisotropic layer, the current density is not parallel to the electric field and gives rise to a different depth dependence. For example, there is a strong concentration of currents in the x direction at the top of the layer producing an enhanced magnetic field in the y direction in the upper uniform layer. At the surface, the magnitudes of the RT ($\boldsymbol{U}_a$) in the x and y directions are appropriate for a homogeneous half-space but the phase tensors (RPT and PT) are more sensitive and respond earlier to the varying resistivity. The origin of this phase behavior is related to the depth dependence of the current density, influenced by the anisotropic layer for both excitations that results in an apparent current density at the surface ($\boldsymbol{J}_a$), which influences both the electric and magnetic field (equation 4). In contrast to the PT ($\boldsymbol{\phi}$), which is driven by changes in the magnetic field, the RPT ($\boldsymbol{\phi}_a$) is driven by changes in the electric field. This is crucial for the explanation of opposite directions of the responding axes of the tensors.

3.3. MT Tensors in 2-D Environments

In this section we add a vertical boundary to our model, which leads to the concept of the TE and TM mode with currents parallel and normal to the surface of the boundary. In the absence of galvanic sources, the conservation of electric charge is a fundamental principle explaining the existence of the TM electric field. The free charge density (q_f, C/m^3) arises wherever the conductivity has a gradient ($\nabla\boldsymbol{\sigma}$) and there is an electric field component in the direction of $\nabla\boldsymbol{\sigma}$. For a discontinuous change in conductivity from σ_1 to σ_2, the conductivity gradient approaches infinity at each side of the boundary and the volumetric free charge density becomes a surface charge density (τ_f, C/m^2) confined to the boundary separating the two regions (Li & Oldenburg, 1991). The surface charge creates a discontinuity in the normal components of the

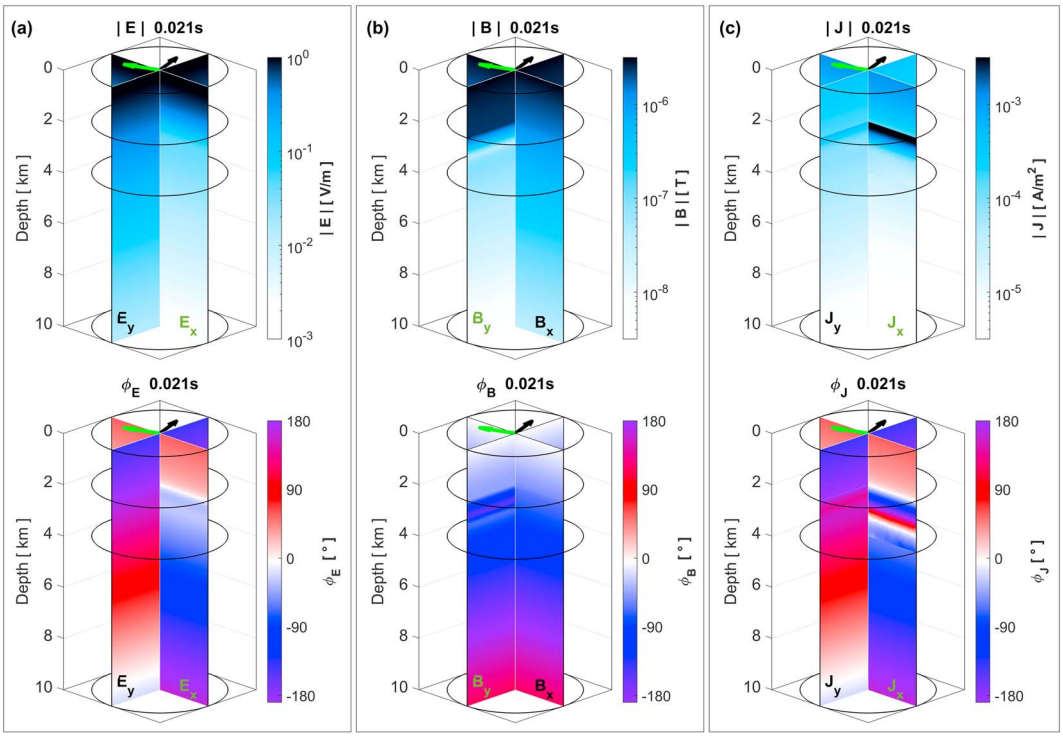

Figure 5. Electromagnetic fields for the anisotropic 1-D model in Figure 4. Magnitude and phase values for (a) electric field, (b) magnetic field, and (c) current density at a period of 0.021 s (47 Hz), for B_x excitation (component names in black letters) and B_y excitation (green letters). The fields in the x and y directions are visualized as perpendicular depth slices. The upper and lower boundaries of the anisotropic body between 2- and 4-km depth are marked by two black circles. The anisotropy directions are indicated by the green (10 Ω m) and black (1,000 Ω m) arrows at 0-km depth.

electric displacement $\boldsymbol{D}$ and the electric field $\boldsymbol{E}$; it maintains the continuity of the normal component of $\boldsymbol{J}$ and results in a refraction of the current density at the respective surface. Following Li and Oldenburg (1991):

$$D_{2n} - D_{1n} = \tau_f \tag{15a}$$

$$E_{2n} - E_{1n} = \frac{\tau_f}{\varepsilon} \tag{15b}$$

$$J_{2n} - J_{1n} = 0 \tag{15c}$$

In the case of quasi-stationary time-varying EM fields, the charge density changes synchronously (i.e., is approximately in phase) with the electric field. The time-varying surface charge distribution on a conductivity interface is given by Kaufman (1985):

$$\tau_f(t) = t_{0s}(\sigma_1 - \sigma_2)\overline{E}_n(t) \tag{16a}$$

$$t_{0s} = \frac{2\varepsilon}{\sigma_1 + \sigma_2} \tag{16b}$$

$$\overline{E}_n = \frac{E_{n1} + E_{n2}}{2} \tag{16c}$$

where $\overline{E}_n$ is the averaged normal component of the electric field at a point on the interface and ε is the electrical permittivity. In the frequency domain (16a) and (16b) can be written as

$$\tau_f(\omega) = -2\,\varepsilon\left(\frac{\sigma_2 - \sigma_1}{\sigma_2 + \sigma_1}\right)\overline{E}_n(\omega) \tag{17}$$

A conducting medium beneath the Earth's surface can be considered as piecewise homogeneous, that is, consisting of different regions of uniform conductivity separated by sharp boundaries, so only

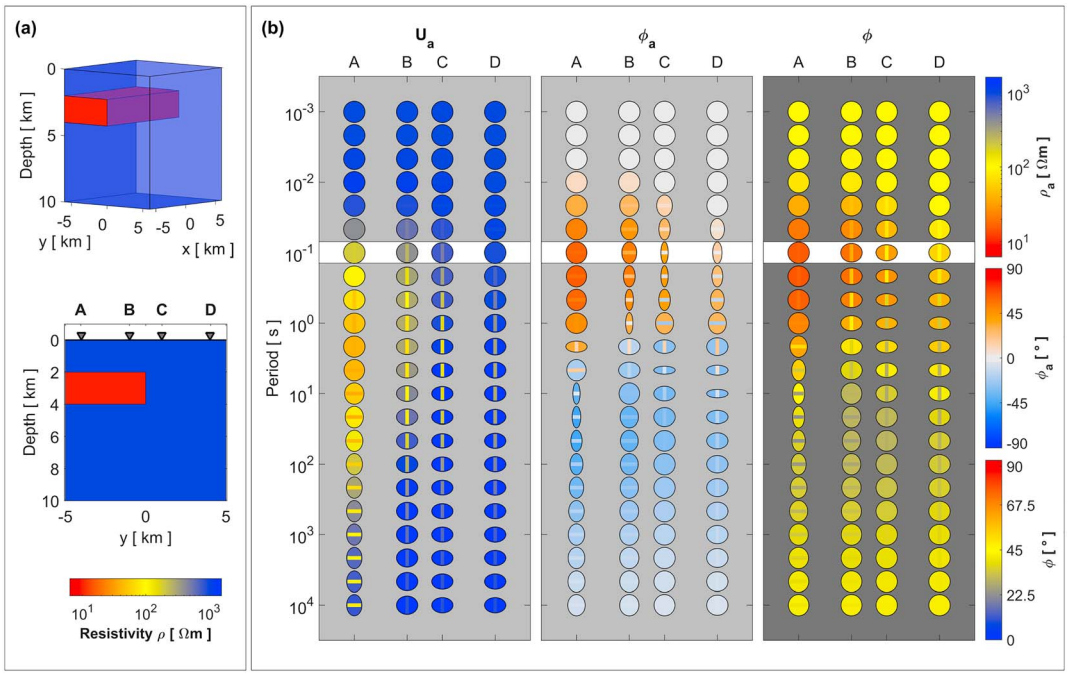

Figure 6. Results for a simple 2-D plate model. (a) Section of the inner part of the model. The plate is 2 km thick, its top is at 2 km depth, and it extends to infinity in the x direction and negative y direction. The location of four observation sites is marked along a profile in y direction (a: −4 km, b: −1 km, c: 1 km, and d: 4 km). (b) Theoretical response for the RT ($\boldsymbol{U}_a$), RPT ($\boldsymbol{\phi}_a$), and conventional PT ($\boldsymbol{\phi}$). The highlighted period is related to the fields shown in Figures 7 and 9.

surface charges arise (Kaufman, 1985). The magnetic fields associated with these charges are negligible because the currents associated with the time-varying charge are the same order of magnitude as the displacement currents, which are neglected in the quasi-stationary assumption for MT (Jones & Price, 1970).

The impact of the vertical boundary and associated charges on the new tensors is investigated using a 2-D plate model consisting of a 2-km-thick conducting plate (10 Ω m) at 2-km depth, which is surrounded by a 1,000 Ω m half-space. The plate is extended to infinity in the x direction and in the negative y direction (Figure 6a). An accurate representation of the EM fields and associated charges requires the discretization of the model to be exceedingly fine (Figure 2b).

$\boldsymbol{U}_a$, $\boldsymbol{\phi}_a$, and $\boldsymbol{\phi}$ are shown at four sites (Figure 6b) along a profile across the vertical boundary (Figure 6a, lower plot). For the shortest periods (0.001–0.01 s) the responses indicate a uniform half-space. From 0.021 to 1 s, Site A approximates a 1-D situation, while Sites B, C, and D show strong 2-D effects, which manifest in a significant split between the major and minor axes of $\boldsymbol{U}_a$, $\boldsymbol{\phi}_a$, and $\boldsymbol{\phi}$. For the RT and the PT the major axes are perpendicular and the minor axes are parallel to the plate boundary; for the RPT it is the opposite. In the period range between 0.1 and 1 s the minor axes of the RPT at Sites C and D take highly negative values, while the major axes are still positive. This coincides with PT major axes above and minor axes below 45°, respectively. With increasing period both principal axes of the PT drop below 45°. Due to the centering of the RPT at 0°, there is an abrupt change in the direction of the minor and the major axes at ~5 s, because here the absolute value of the negative axes (perpendicular to the boundary) becomes larger than the value of the positive axes (parallel to the boundary). For periods between 2.1 and 100 s, 2-D effects are also observed at Site A. Below 10 s both principal axes (at all sites) of $\boldsymbol{\phi}_a$ and $\boldsymbol{\phi}$ are smaller than 0° and 45°, respectively. Toward the longest periods, $\boldsymbol{U}_a$, $\boldsymbol{\phi}_a$, and $\boldsymbol{\phi}$ again approximate a uniform half-space, except for $\boldsymbol{U}_a$ at Site A where the tensor split persists.

3.3.1. Tensors, Fields, and Charges in the TM Mode

In Figure 7, the magnitudes and phases of the magnetic, electric, and current density fields at a period of 0.1 s are shown for the TM mode related to the plate model in Figure 6. In this mode the magnetic fields are parallel to the plate boundary (B_x) and electric fields cross the boundary (E_y). The latter results in induced

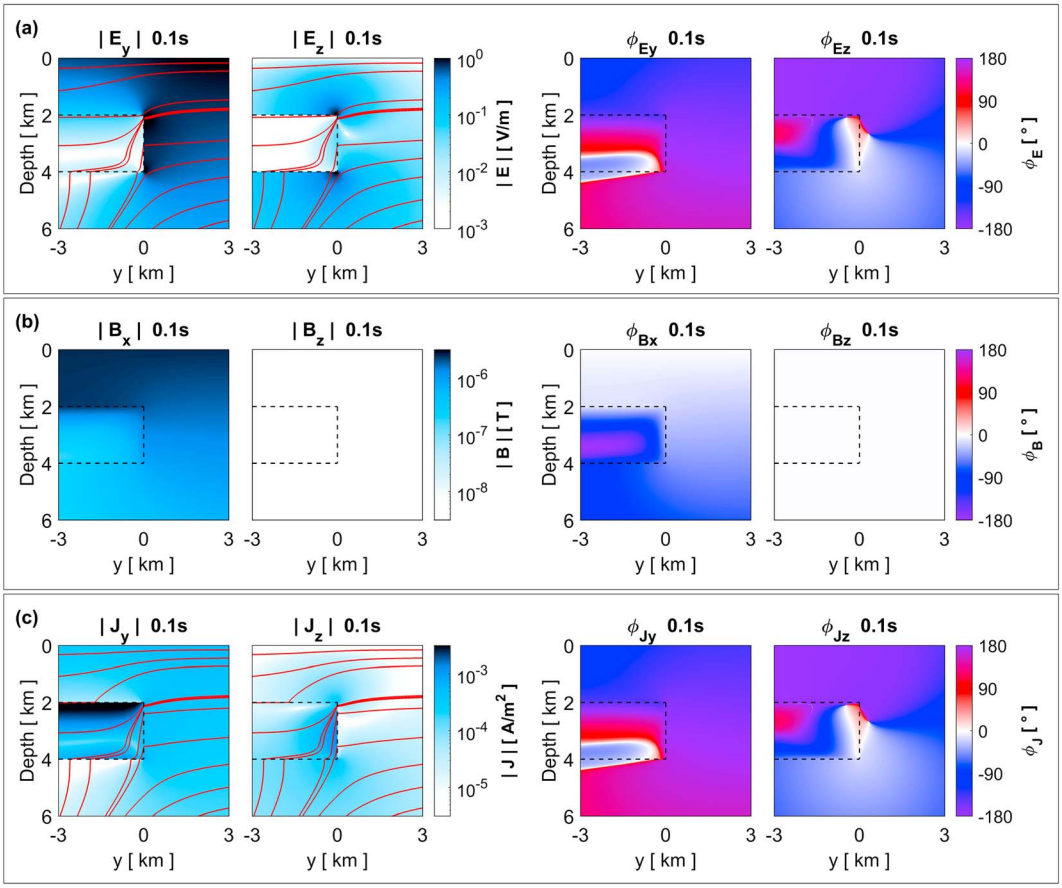

Figure 7. Magnitudes and phases of the EM fields at a period of 0.1 s in the TM mode for the 2-D plate model from Figure 6. (a) Electric fields (E_y and E_z) and streamlines. (b) Magnetic fields (B_x and B_z). (c) Current density (J_y and J_z) and its streamlines. There are significant vertical E_z and J_z but no B_z (no tipper vectors).

galvanic currents with horizontal and vertical components (J_y, J_z). In Figures 7a and 7c, the streamlines of the electric field and the current density, plotted on top of the magnitudes, illustrate how the currents are concentrated in the conducting plate at the upper and vertical boundaries. To maintain the continuity of the normal component of $\boldsymbol{J}$, surface charges build at the vertical boundary. The boundary therefore resembles a charged plane, involving a secondary electric field with components in the y and z directions. The magnetic field in the TM mode is more homogeneous and has no vertical component, consistent with the assumption that the magnetic field related to the boundary charges is negligible. The horizontal magnetic field phase ($\boldsymbol{\phi}_{Bx}$) at the surface is 0° and complicated near the conducting anomaly. The electric field phase ($\boldsymbol{\phi}_{Ey}$) changes at and across the plate boundary surfaces and therefore causes differences in $\boldsymbol{\phi}$ and in $\boldsymbol{\phi}_a$ for sites above and next to the conductor.

The magnetic field (B_x) at the surface is constant along the y axis, but the electric field (E_y) decreases with depth for sites above the conductor. While the behavior of the fields beneath Site A resembles that within a 1-D half-space, only the magnetic field component shows a decay governed by the underlying depth-dependent resistivity. The magnitudes and phases of the electric and current density field components are strongly influenced by the charges on the vertical boundary. For $\boldsymbol{\phi}_a$, these variations result in highly negative minor axes perpendicular to the plate boundary (and coincidentally large major axes for the TE mode) in the respective period range between 0.1 and 1 s. The effects are also observed by PT values below 45°, but they are distinctly less significant.

The surface charge density (τ_f) according to (17) is presented at the surfaces of the plate for two different target periods (Figure 8a). As the fields pass from a resistor to a conductor, the sign of τ_f is negative. Depending on the period-dependent penetration depths, the charges are dominant on the upper edge for 0.021 s and at

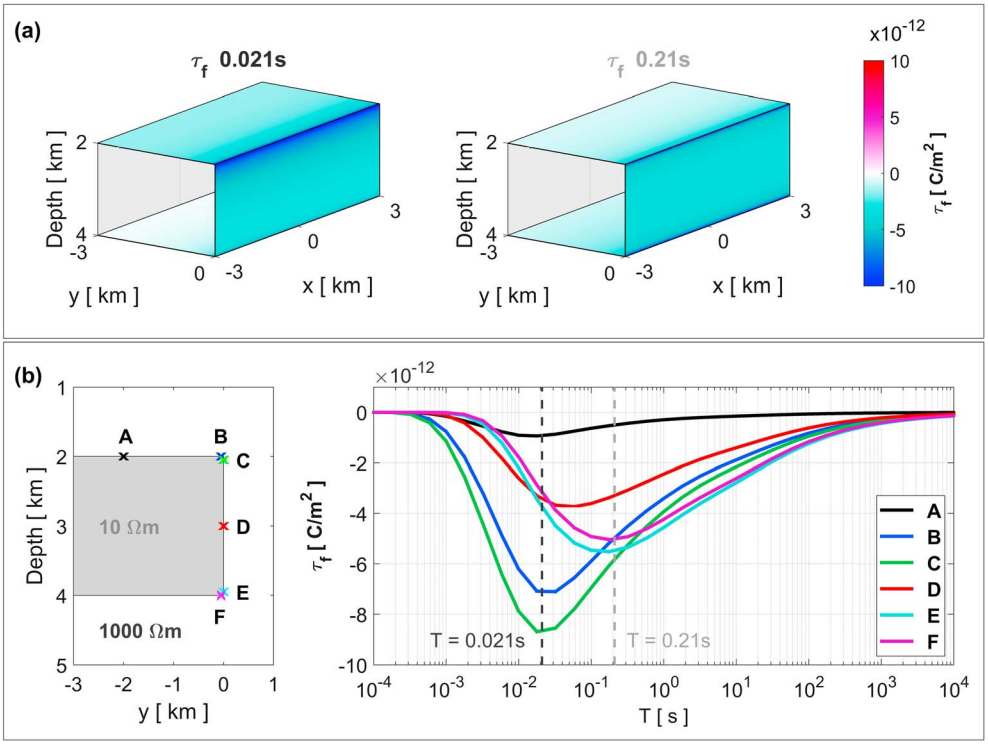

Figure 8. Surface charge density (τ_f) at the boundaries of the 2-D plate model from Figure 6. (a) The surface charge density is visualized at the surfaces of the conducting plate for two periods (0.021 and 0.21 s). As the fields pass from a resistor to a conductor, the charge density is negative. In general, the charges are dominant on the vertical surface with a maximum close to the edges. (b) The surface charge density is shown for six points at (a) −2 km, −2 km; (b) −0.05 km, −2 km; (c) 0 km, −2.05 km; (d) 0 km, −3 km; (e) 0 km, −3.95 km; and (f) −0.05 km, −4 km. The maximal amplitude of the charge density is dependent on the depth and the period. The plots in (a) are chosen for periods where the charge density amplitude is maximum at the upper and the lower plate edge, respectively.

the upper and lower edges for 0.21 s. On the upper and lower plate surfaces, charges accumulate close to the edges but they decrease quickly with increasing distance from the vertical boundary. In Figure 8b the period-dependent charge accumulation is shown at six different locations (A–F) on the plate boundary. At the upper edge there is a maximum of the charge density at 0.021 s and at the lower edge at 0.21 s (Figure 8a). At A, 2 km from the vertical boundary, the charge density is small at all periods. For periods longer than 0.21 s, τ_f decreases at all points on the plate and vanishes for the longest periods. These findings imply that the observed tensor responses in the TM mode are highly influenced by charge accumulation in the period range from 0.001 s to approximately 100 s.

3.3.2. Tensors and Fields in the TE Mode

In the TE mode the electric (E_x) and current density fields (J_x) are parallel to the vertical plate boundary so charges do not build up and the observed effects are similar to 1-D induction above different subsurface conditions. The EM fields have different penetration depth depending on the location along the y axis. The TE mode includes a vertical magnetic field (B_z) but B_z is not directly related to any charges at the vertical boundary. The magnitudes and phases of the E, B, and J components are shown (Figure 9) for the TE mode for a period of 0.1 s. The magnitude of the electric field (E_x) at the surface above the plate is decreased and that of the magnetic field (B_y) is enhanced due to the currents accumulated at the upper plate boundary (J_x). This leads to a decrease in $\boldsymbol{U}_a$ for the tensor component parallel to the boundary (x direction). For sites above the resistive half-space, the magnetic field decreases and the electric field increases. $\boldsymbol{U}_a$ is parallel to the boundary and therefore increases with increasing distance to the vertical boundary. The electric field phase (ϕ_{Ex}) at the surface is larger above the conductor than above the resistor. This links directly to the PT component perpendicular to the boundary and the RPT component parallel to the boundary, which are both

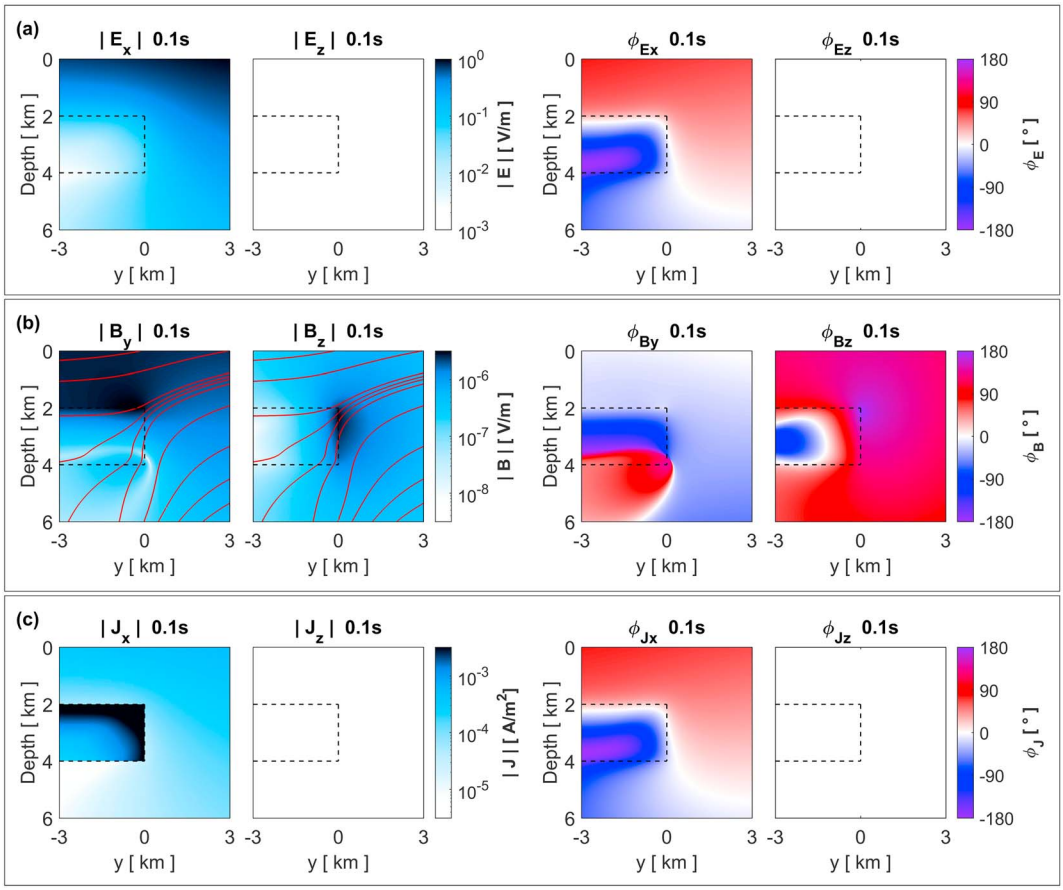

Figure 9. Magnitudes and phases of the EM fields at a period of 0.1 s in the TE mode for the 2-D plate model from Figure 6. (a) Electric fields (E_x and E_z). (b) Magnetic fields (B_y and B_z) and its streamlines. (c) Current density (J_y and J_z). There is a strong B_z but no E_z or J_z.

larger above the conductor than beside it. Similar to the 1-D isotropic and anisotropic cases, the variation in $\boldsymbol{\phi}_a$ is more distinct than in $\boldsymbol{\phi}$.

3.4. Conclusions on the Forward Modeling Studies

Each of the components of the CART, $\boldsymbol{U}_a$, $\boldsymbol{V}_a$, and $\boldsymbol{\phi}_a$, and the phase tensor, $\boldsymbol{\phi}$ can be represented as ellipses (cf. Figure 1). The RT quantifies the apparent dissipative behavior of the electric field as it diffuses through the resistive subsurface (Brown, 2016), and for a given period, the tensor is sensitive to the resistivity in a region below the observation point where most of the electric current is focused. The RPT (and similarly $\boldsymbol{V}_a$) quantifies an additional spatial dispersion associated with the phase relationships between the electric field and apparent current density. It is represented by an ellipse with a major axis indicating the horizontal direction of the maximum apparent induction current density, associated with the *horizontal gradient* of the resistivity in the region where most of the electric current is focused. The PT ellipse has similar properties where the direction of its major axis points toward the preferred flow direction of the induction current, similar to the real part of the vertical magnetic transfer function (Caldwell et al., 2004).

The results for the 1-D forward model in section 3.1 demonstrate the high sensitivity of the RT and the RPT to vertical resistivity gradients, which might improve the ability to resolve thin conductive layers. Period-dependent RPT curves can be interpreted like conventional PT curves. Their uniform half-space value is 0°; phases above 0° imply a transition from a resistor to a conductor, and negative phases occur if the fields pass into a resistor.

In anisotropic 1-D environments (section 3.2), the RT principal axes align with the anisotropy directions. The imaginary part of the CART is sensitive to resistivity gradients and is directly related to the RPT. In

contrast to the PT, which relates the magnetic to the electric field, the RPT relates the electric field to the apparent current density vector. As a consequence, the axes of the RPT and the PT, which are sensitive to the resistivity gradient in the conductive anisotropy direction, are orthogonal. The RPT response is more pronounced than the PT.

The 2-D plate model (section 3.3) introduced the tensors in the TM- and the TE mode. For the CART and the RPT, the TM mode relates to the tensor axes perpendicular to the plate boundary and for the PT to the axes parallel to the plate boundary. For the TE mode it is the opposite. In the TM mode the charges at the vertical resistivity boundary cause a strong secondary electric field. For a conductive anomaly this generates negative RPT minor axes, which reflect the high sensitivity of the RPT to horizontal resistivity gradients.

4. 3-D Inversion with Apparent Resistivity Tensors

The previous sections demonstrate that the CART ($\boldsymbol{\rho}_a$) and the RPT ($\boldsymbol{\phi}_a$) have a high sensitivity to horizontal and vertical resistivity gradients. This might be of benefit in 3-D inversion schemes, especially for the resolution of horizontal and vertical boundaries. To test this hypothesis, the new tensors were incorporated into the 3-D inversion code ModEM (Kelbert et al., 2014). The focus of this study is the comparison with the MT response tensor ($\boldsymbol{Z}$) and PT ($\boldsymbol{\phi}$) inversion results for the well-investigated synthetic 3-D oblique conductor model (Ledo, 2006; Tietze et al., 2015).

4.1. ModEM Adaption, Inversion Setup, and Data Errors

The ModEM inversion software (Kelbert et al., 2014) is based on a nonlinear conjugate gradient algorithm, which minimizes the penalty function $\psi = \psi_d + \lambda\psi_m$, where ψ_d is the data regularization term, ψ_m the model regularization term, and λ the trade-off parameter (Egbert & Kelbert, 2012).

Besides including the calculation of the forward response, it is necessary to include the calculation of the data sensitivities for the new tensors, that is, the change in the theoretical response with respect to changes in the model resistivity. Similar to the calculation of PT sensitivities (Patro et al., 2013; Tietze et al., 2015), the sensitivity calculations for $\boldsymbol{U}_a$, $\boldsymbol{V}_a$, and $\boldsymbol{\phi}_a$ can be accomplished using a linear combination of the MT response tensor sensitivities and the derivatives of $\boldsymbol{U}_a$, $\boldsymbol{V}_a$, or $\boldsymbol{\phi}_a$ with respect to the real and imaginary components of $\boldsymbol{Z}$ (U_{ij} and V_{ij}, $ij = 1,2$). The sensitivities, with respect to the electric field on the model grid (e), are calculated using the chain rule (Tietze et al., 2015):

$$\frac{\partial \chi_{ij}}{\partial e} = \frac{\partial \chi_{ij}}{\partial Z_{ij}}\frac{\partial Z_{ij}}{\partial e} = \frac{\partial \chi_{ij}}{\partial U_{ij}}\frac{\partial U_{ij}}{\partial e} + \frac{\partial \chi_{ij}}{\partial V_{ij}}\frac{\partial V_{ij}}{\partial e}; \tag{18}$$

where $\boldsymbol{\chi}$ represents either $\boldsymbol{U}_a$ or $\boldsymbol{V}_a$ or $\boldsymbol{\phi}_a$. A detailed derivation of the sensitivities is given in Appendix B.

The oblique conductor model is composed of a regional 2-D structure, represented by two quarter spaces of 500 and 50 Ω m and an oblique 3-D structure of 5 Ω m (Figure 10a). The quarter spaces are located in a depth range between 0.1 and 71 km; the conductor is rotated by 45° from the x axis; it has a dimension of $9 \times 9 \times 30$ km^3 and is located at 2.56-km depth. The model is covered by a 100-m-thick layer with a resistivity of 100 Ω m.

For comparison with existing results, the forward response, which served as input to the inversion, was calculated using the ModEM forward solver. The inner model domain had a horizontal extension of 50×50 km^2 and was discretized by a 1 km × 1 km mesh. In the outer model, the horizontal mesh element size was increased by a factor of 1.2, until a total model size of 500 km was reached. In the vertical direction the surface cell size was 0.02 km and was increased by a factor of 1.2 to a depth of 500 km. The inner model used for the forward calculation is shown in Figure 10b. Subsequently, the forward response was calculated for a site array of 10 × 10 sites with a site spacing of 4 km (Figure 10a). The forward response is shown (Figure 11) for $\boldsymbol{U}_a$, $\boldsymbol{V}_a$, $\boldsymbol{\phi}_a$, and $\boldsymbol{\phi}$ at all sites for three representative periods (0.1, 1, and 100 s). At 0.1 s the tensors mainly indicate a 1-D situation, but 2-D and 3-D effects are already present with clear splits in the principle axes of $\boldsymbol{V}_a$ and $\boldsymbol{\phi}_a$. $\boldsymbol{U}_a$ demonstrates distinctly the different resistivity values above the two quarter spaces. The responses at 1 s are dominated by 2-D and 3-D effects, while for 100 s the horizontal 2-D structure becomes dominant for the entire data set. Prior to inversion, Gaussian noise was added to the synthetic data, in accordance with the definition of the data errors.

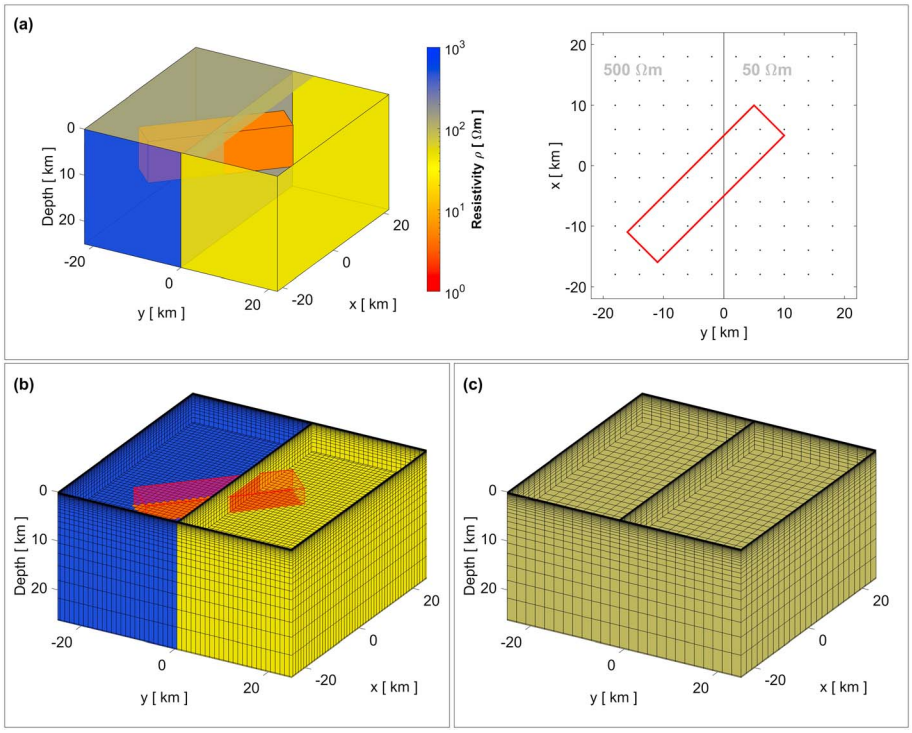

Figure 10. Three-dimensional resistivity model. (a) Geometry, resistivity (left), and site array (right). (b) Finite differences (FD) mesh with resistivity values for the calculation of the forward response in ModEM. The mesh is shown for the inner part of the model and only at selected surfaces. (c) Inner part of the FD mesh used for the inversion in ModEM. The mesh is very fine at the surface and becomes coarser with depth. In the horizontal direction the grid is a factor of 2 coarser than the forward calculation grid. The resistivity of the starting model is 100 Ω m.

The inversion grid was chosen to be the same as for the forward model, except for the horizontal cell spacing in the inner model, which was set to 2 km (Figure 10c).

For field data, it is convenient to calculate tensor errors using the delta method (Efron, 1982) under consideration of the error covariance (Booker, 2014). Nevertheless, for this study we followed Tietze et al. (2015) and Miensopust (2017) and defined the data errors relative to the individual tensor amplitudes. We set the errors to 3% of $|\boldsymbol{\phi}_{ij}|$ and 3% of $|\boldsymbol{\phi}_{a,ij}|$ in combination with a floor of 0.03 for PT and RPT. MT response tensor errors were set to 3% of $|\boldsymbol{Z}_{ij}|$ in combination with a floor of 3% of $|Z_{xy} \times Z_{yx}|^{1/2}$. Finally, the errors for $\boldsymbol{U}_a$ and $\boldsymbol{V}_a$ were defined to be 3% of $|\boldsymbol{\rho}_{a,ij}|$. Several empirical inversion tests yielded an optimal error floor of 5 Ω m for both, $\boldsymbol{U}_a$ and $\boldsymbol{V}_a$.

4.2. Inversion Results

We used a covariance smoothing of 0.3 in *x*, *y*, and *z* directions and present inversion results from a starting model of 100 Ω m. The influence of the starting model on the inversion results is directly related to the model regularization scheme, which in the case of ModEM is based on differences between the current model and the a priori model (e.g., Siripunvaraporn & Egbert, 2000). This is important, especially for the PT and the RPT inversions, which lack information about absolute resistivity values. Tietze et al. (2015) concluded that inversion results are most accurate if the prior model resistivity is close to the regional average of the subsurface resistivity. Further tests concerning the prior model are not part of this study.

The inversion results are shown (Figure 12) for five different inversion input parameters: MT response tensor ($\boldsymbol{Z}$), CART ($\boldsymbol{\rho}_a$), PT ($\boldsymbol{\phi}$), RPT ($\boldsymbol{\phi}_a$), and a joint inversion between RT ($\boldsymbol{U}_a$) and RPT. The inversion of $\boldsymbol{\rho}_a$ was implemented by performing a joint inversion of $\boldsymbol{U}_a$ and $\boldsymbol{V}_a$.

The results are presented for five different depth slices (0.05, 0.9, 2.8, 5, and 15 km) and a vertical profile in the strike direction of the conductor (Figure 12). The PT inversion is similar to the result from Tietze et al.

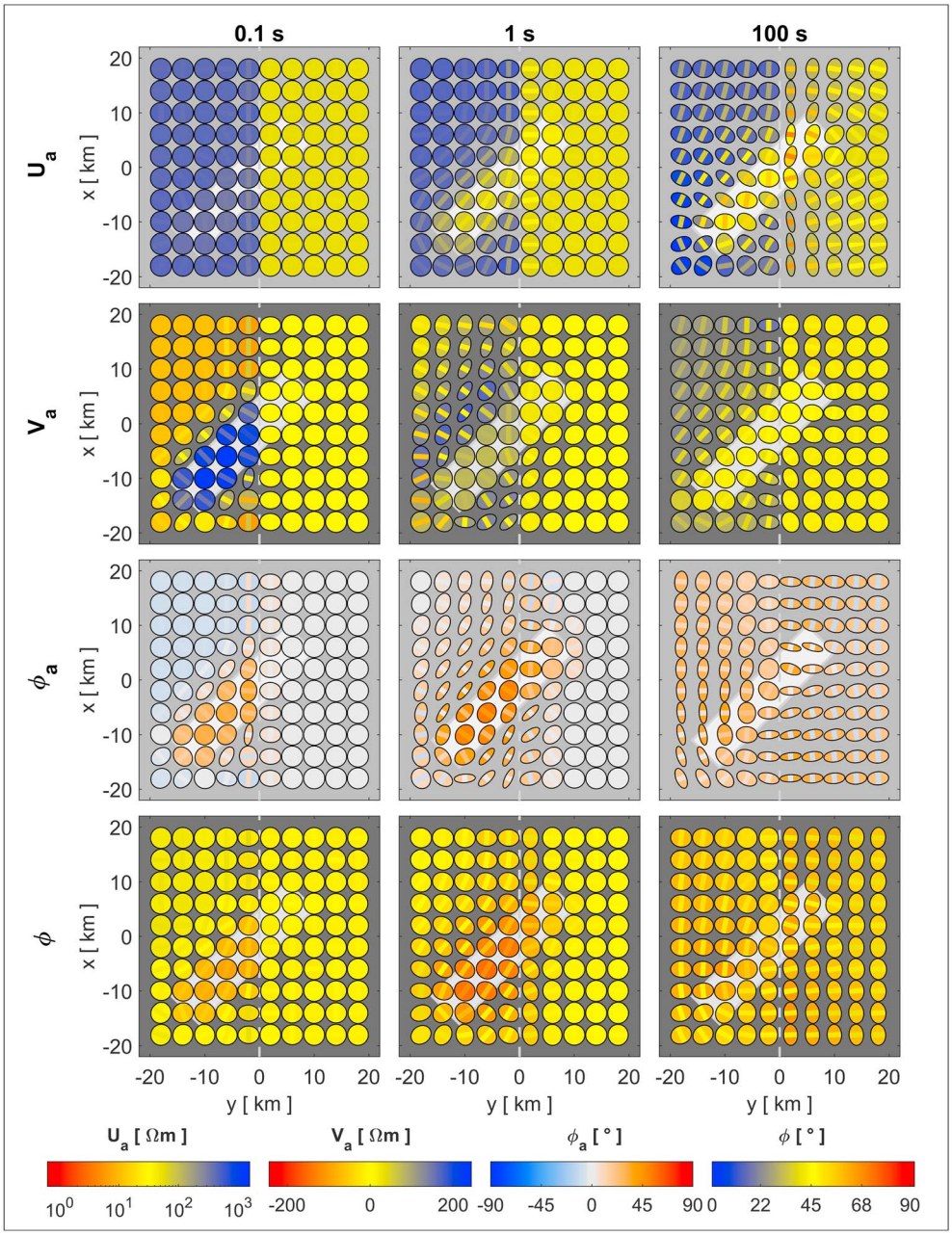

Figure 11. Responses from the forward calculation with ModEM. The RT ($\boldsymbol{U}_a$), imaginary part of the CART ($\boldsymbol{V}_a$), RPT ($\boldsymbol{\phi}_a$), and conventional PT ($\boldsymbol{\phi}$) are shown for three periods, 0.1, 1, and 100 s.

(2015) with a 100 Ω m prior model and no vertical magnetic field transfer functions. As our focus is on the conductive anomaly, we show our results in a smaller resistivity range.

The inversion results are all very good, and all parameters converged to the target RMS of 1.00. Nevertheless, there are differences in the models. The RPT and PT inversions both have difficulties in reproducing the resistive quarter space, most obviously in the case of the RPT inversion. Here, the lack of information about the absolute resistivity causes the inversion algorithm to generate a conductor close the surface (the upper left part of the model space) to reproduce the resistivity gradient observed in the RPT and PT responses. The high sensitivity of the RPT seems to enhance this effect. With regard to the resolution of the conductor, the RPT yields a slightly more homogeneous response with a stronger contrast to the 50 Ω m quarter space, but the differences are very small. For an inversion with the MT response tensor ($\boldsymbol{Z}$), the quarter spaces are

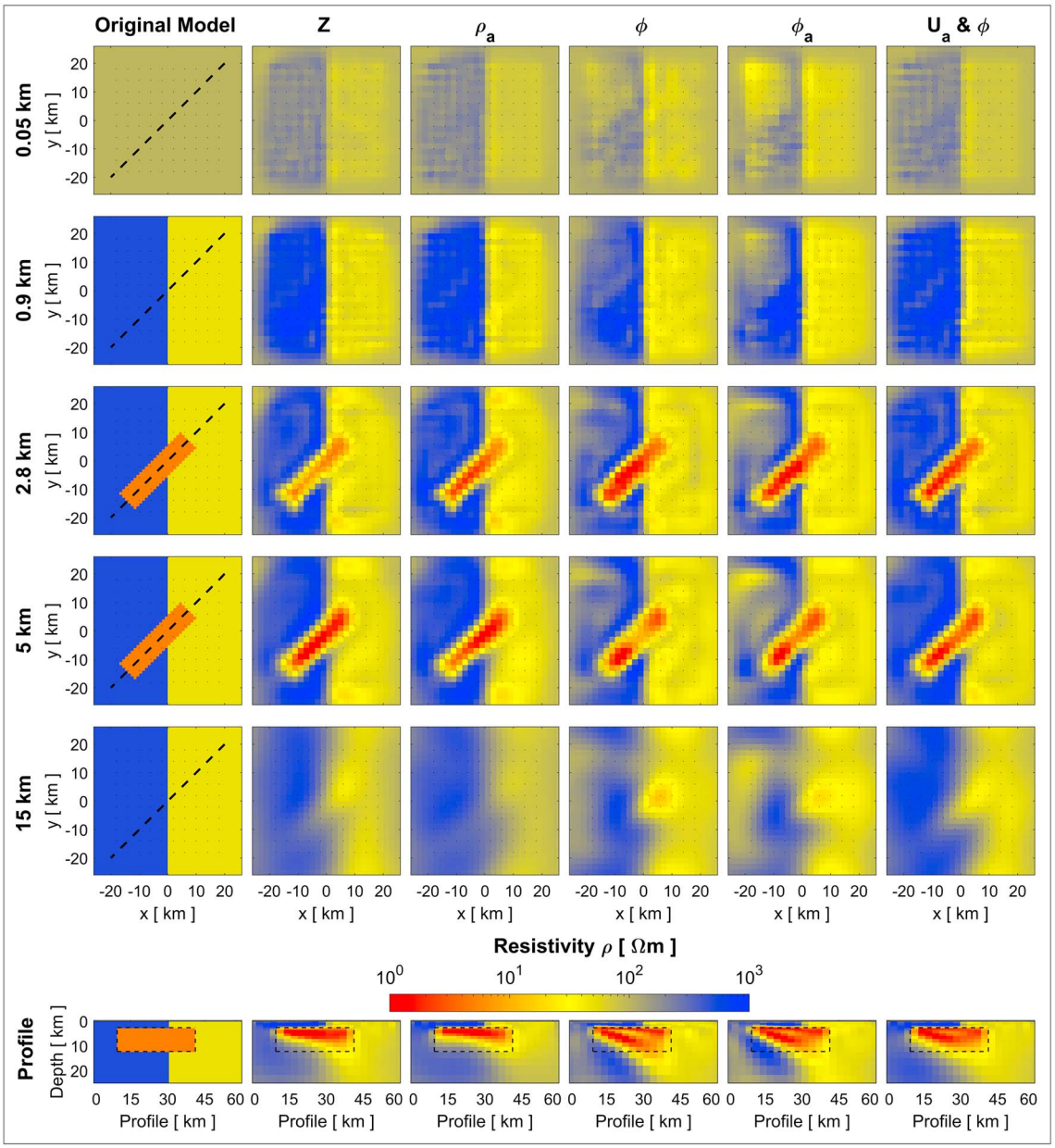

Figure 12. Inversion results from a starting model of 100 Ω m. The left column shows the original model, and the other columns show results for inversions with different input parameters. The rows contain the model resistivity at different depths slices and along a vertical depth section whose location is indicated by the dashed line.

well resolved, but the upper surface of the conductor (2.8-km depth) is not well defined. This is better for the inversion using $\boldsymbol{\rho_a}$, but here the 50 Ω m quarter space at depth (15-km slice) produces resistivity values that are too high. The resolution of the lower boundary of the conductor is more distinct for an inversion on $\boldsymbol{\rho_a}$ compared with one on $\boldsymbol{Z}$. This can be seen in the vertical profile, where the distinction between the conductor and the underlying quarter spaces is closer to a horizontal boundary for the inversion with $\boldsymbol{\rho_a}$. On the other hand, the thickness of the conductor is underestimated by the inversion with $\boldsymbol{\rho_a}$; this coincides with an underestimation of the absolute resistivity value of the conductor so producing a conductance close to the true conductance value. The CART results are in good agreement with the stronger response to horizontal boundaries for $\boldsymbol{\rho_a}$ compared to $\rho_{a,Z}$ (section 3.1).

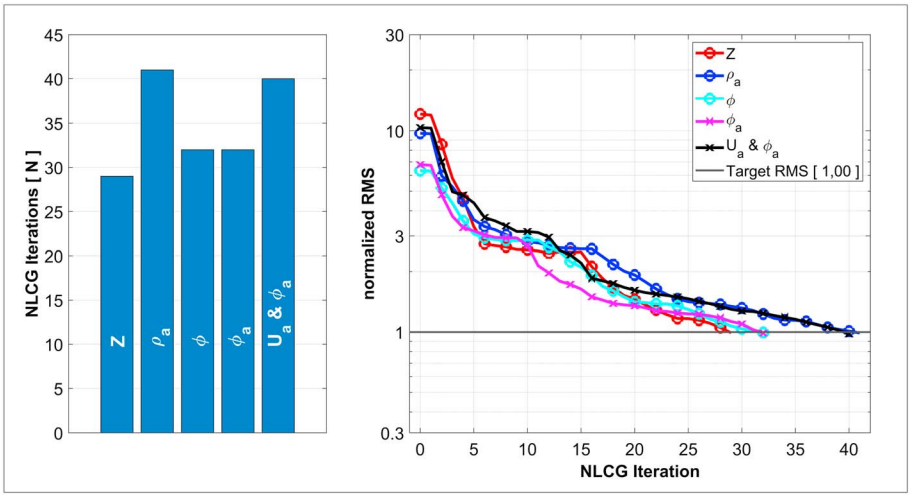

Figure 13. The left plot shows the number of nonlinear conjugate gradient iterations for the five different inversion approaches. The inversion with the MT response tensor ($\boldsymbol{Z}$) is most efficient and takes less than 30 iterations. $\boldsymbol{\phi}_a$ and $\boldsymbol{\phi}$ are equally efficient (32 iterations), the inversions for $\boldsymbol{U}_a$ with $\boldsymbol{\phi}_a$ and for the CART ($\boldsymbol{\rho}_a$) take the longest (40 and 41 iterations). The right plot shows the convergence performance for the five approaches.

The best inversion result is achieved by a joint inversion of $\boldsymbol{U}_a$ with $\boldsymbol{\phi}_a$. The quarter spaces are reproduced, the boundaries of the conductor are well defined (vertically and horizontally), and the location of the lower boundary is in very good agreement with the true model. Here, the strong response to horizontal boundaries in the amplitude information in $\boldsymbol{U}_a$ complements the high sensitivity of $\boldsymbol{\phi}_a$ to vertical resistivity boundaries (section 3.3).

The quality of each inversion is expressed by L_ρ, that is, the differences between the logarithmic resistivities of the inversion model (ρ_{inv}) and the true model (ρ_{true}):

$$L_\rho = \sqrt{\frac{\sum_{i=1}^{N} \left(\log_{10}(\rho_{\text{inv},i}) - \log_{10}(\rho_{\text{true},i})\right)^2}{N}} \tag{19a}$$

with $i = 1 : N$ for inversion cells located in the inner ($50 \times 50 \times 80$ km^3) model domain. It yields a value of 0.316 in case of the inversion for $\boldsymbol{U}_a$ together with $\boldsymbol{\phi}_a$, which is superior to the results from $\boldsymbol{Z}$ (0.344), $\boldsymbol{\rho}_a$ (0.344), $\boldsymbol{\phi}$ (0.384), and also $\boldsymbol{\phi}_a$ (0.425).

A visual interpretation of the inversion results (Figure S4 in the supporting information) demonstrates the deviation of the inversion models (ρ_{inv}) from the true model (ρ_{true}) for each inversion cell by calculating:

$$\Delta\rho = \frac{\log_{10}(\rho_{\text{inv}}) - \log_{10}(\rho_{\text{true}})}{\log_{10}(\rho_{\text{true}})} \cdot 100 \tag{19b}$$

The inversions were calculated on a server with 2 CPUs (12 cores at 2GHz) and 96-GB internal memory. Computation times ranged between 20 hr for an inversion on $\boldsymbol{Z}$ and 27 hr for $\boldsymbol{\rho}_a$. The convergence performance and count of nonlinear conjugate gradient iterations of the different input parameters demonstrates (Figure 13) that an inversion on $\boldsymbol{Z}$ is more efficient than all other inversion parameters. ModEM offers several methods for tuning the inversion process, and the default settings are optimized for an inversion on $\boldsymbol{Z}$. Nevertheless, the convergence of the new tensors is good and there may be room for improvement in the future.

The visualization of the tensor misfit (Figure 14) is similar to that of Cembrowski and Junge (2018), who follow Booker (2014) by taking the absolute difference between the observed (χ_{obs}, inversion input) and the predicted (χ_{pred}, inversion output) tensors ($\chi = \boldsymbol{U}_a, \boldsymbol{V}_a, \boldsymbol{\phi}_a, or\ \boldsymbol{\phi}$). Here, we show the differences of the tensor principal axes magnitude ($\chi_{\max}$, $\chi_{\min}$) and the difference in the magnitude of the rotation angle ($\alpha - \beta$).

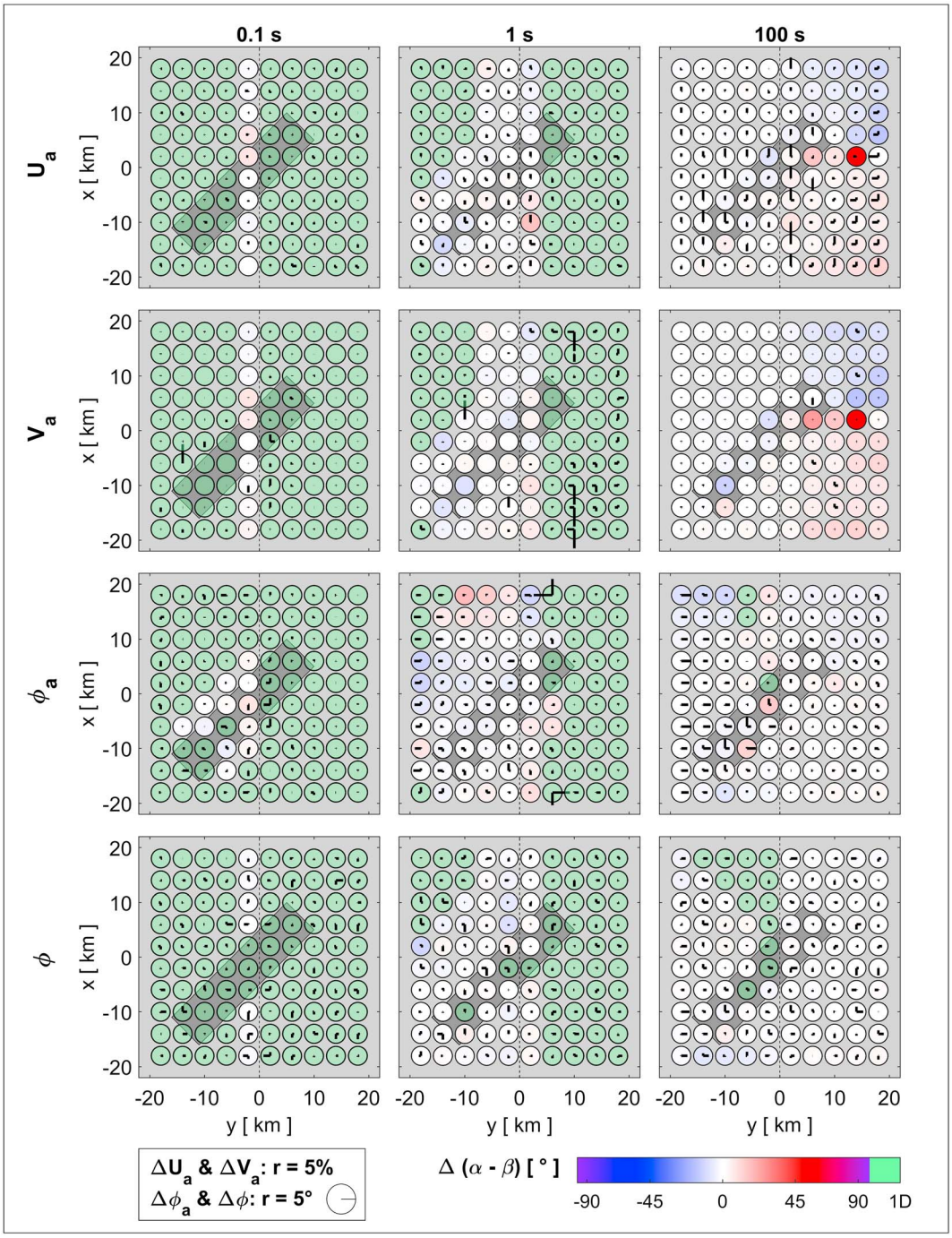

Figure 14. Tensor deviations between responses from the inversion model and input data. The color of the circles indicates the misfit of the rotation angle ($\alpha - \beta$). The green color denotes 1-D situations where the direction of the tensors is undefined. The radius (r) of the circles marks a relative error of 5% in the case of $\boldsymbol{U}_a$ and $\boldsymbol{V}_a$ and an absolute error of 5° for $\boldsymbol{\phi}$ and $\boldsymbol{\phi}_a$. The bars within the circles are scaled to the individual tensor axes errors (vertical bars: major axis, horizontal bars: minor axis). Horizontal or vertical bars crossing the circles imply errors larger than 5% or 5°, respectively. The misfit plots of $\boldsymbol{U}_a$ and $\boldsymbol{\phi}_a$ refer to the joint inversion of $\boldsymbol{U}_a$ and $\boldsymbol{\phi}_a$ and the plots of $\boldsymbol{V}_a$ to the inversion on $\boldsymbol{\rho}_a$.

The color of the circles indicates the misfit of the rotation angle. A green color denotes 1-D situations where the direction of the tensors is arbitrary. By definition, this is the case if $\phi_{\max} - \phi_{\min} < 5°$, $\phi_{a,\max} - \phi_{a,\min} < 5°$, or $U_{a,\max} - U_{a,\min} < 0.03 \cdot U_{a,\max}$. The radius of the circles marks a relative error of 5% in case of $\boldsymbol{U}_a$ and $\boldsymbol{V}_a$ and an absolute error of 5° in the case of $\boldsymbol{\phi}$ and $\boldsymbol{\phi}_a$. The bars within the circles are scaled to the individual

tensor axes errors (vertical bars: major axis, horizontal bars: minor axis). Hence, horizontal or vertical bars crossing the circles imply errors larger than 5% or 5°, respectively. The fit is shown at three periods (0.1, 1, and 100 s) and refers to the joint inversion of $\boldsymbol{U}_a$ and $\boldsymbol{\phi}_a$, the inversion of $\boldsymbol{\rho}_a$ ($\boldsymbol{V}_a$ is shown), and the inversion of $\boldsymbol{\phi}$. The overall fit is very good and is mostly restricted to slight deviations in the major axis direction and some major axis errors for $\boldsymbol{V}_a$ at 1 s exceeding 5%. In addition, the inversion responses are shown in the supporting information (Figure S5) and can be directly compared with tensors in Figure 11.

The previous results show a distinct improvement in resolving the boundaries of the conductive anomaly using the new tensors. Nevertheless, there are several aspects that need to be investigated in future work, such as more complex canonical models with two overlying conductors to explore the resolution of their upper and lower boundaries. There is the application to real (noisy) data sets and the incorporation of the distortion theory in Brown (2016) with the associated possibility of variable background resistivity for optimized starting models. In addition, the utility of including vertical magnetic transfer functions in a joint inversion with $\boldsymbol{U}_a$ and $\boldsymbol{\phi}_a$ or exclusively $\boldsymbol{\phi}_a$ needs to be tested.

5. Conclusions

We have introduced the complex apparent resistivity tensor (CART, $\boldsymbol{\rho}_a$) and its associated apparent resistivity tensor (RT, $\boldsymbol{U}_a$) and resistivity phase tensor (RPT, $\boldsymbol{\phi}_a$) in multidimensional environments. The tensors provide insight into the complex apparent resistivity distribution of an MT data set. We showed by reference to a 1-D model that the RT and the RPT have a stronger response to vertical resistivity gradients than the conventional apparent resistivity and phase. In anisotropic environments, $\boldsymbol{U}_a$ provides information about the direction of the principal axes and corresponding resistivity. In higher dimensional environments, vertical boundaries become significant. This was demonstrated for a 2-D plate model with a study of the EM fields in the TM- and the TE mode. In the TM mode charges at the vertical surface generate a strong RPT response, which makes it a suitable measure for horizontal resistivity changes. The new tensors bring a significant improvement to the interpretation of MT data, as they provide a compact and comprehensive method to visualize amplitude and phase information contained within the common MT transfer functions. The distinct response to resistivity contrasts, especially for the RPT, allows for immediate conclusions on subsurface structures and dimensionalities, prior to computationally expensive inversions. They also facilitate the selection and setup of appropriate modeling/inversion approaches.

The new tensors have been successfully incorporated into the ModEM code for a synthetic inversion study based on the oblique conductor model (Tietze et al., 2015). All inversion parameters converged successfully to the target RMS of 1.00 and have a satisfactory fit. Although the MT response tensor ($\boldsymbol{Z}$) is best in terms of convergence speed, the speed performance of the new tensors is adequate. With regard to the inversion model quality, the RPT and PT inversions are hampered when reproducing background resistivity values (the quarter spaces), especially for the RPT. The comparison between the inversion for $\boldsymbol{Z}$ and the inversion for $\boldsymbol{\rho}_a$ revealed advantages for $\boldsymbol{Z}$ when reproducing the quarter spaces but also showed the superiority of $\boldsymbol{\rho}_a$ when resolving horizontal boundaries. The best model resulted from an inversion of $\boldsymbol{U}_a$ with $\boldsymbol{\phi}_a$. Here, the high sensitivity to horizontal and vertical boundaries resulted in an excellent recovery of the oblique conductor and rendering of the surrounding quarter spaces. Hence, inverting for $\boldsymbol{U}_a$ and $\boldsymbol{\phi}_a$ might pose an alternative to the inversion for $\boldsymbol{Z}$, although more complex studies have to be realized to test this hypothesis.

Appendix A

The calculation of the tensor ellipse parameters is performed according to Booker (2014, Appendix 1) who determines the correct quadrant and directions of the principal components by comparing the tensor to a unit vector that circles clockwise around a unit circle. The proceeding is crucial as the RPT and the imaginary part of the CART feature negative major and/or minor axes.

Applying a tensor χ (representing either $\boldsymbol{U}_a$,$\boldsymbol{V}_a$, $\boldsymbol{\phi}_a$, or $\boldsymbol{\phi}$) to a family of radial vectors $\boldsymbol{c}(\omega)$, which circle clockwise around a unit circle, creates a second family of radial vectors $\boldsymbol{p}(\omega)$:

$$\mathbf{p}(\omega) = \boldsymbol{\chi}_{\text{ell}}\, \mathbf{c}(\omega) = \begin{pmatrix} \chi_a & 0 \\ 0 & \chi_b \end{pmatrix} \mathbf{R}(\psi)\, \mathbf{c}(\omega) \tag{A1.1}$$

$$\boldsymbol{R}(\psi) = \begin{pmatrix} \cos\psi & \sin\psi \\ -\sin\psi & \cos\psi \end{pmatrix} \tag{A1.2}$$

Here, $\boldsymbol{\chi}_{ell}$ represents the tensor in a coordinate system aligned with the tensor principal axes and $|\chi_a|$ and $|\chi_b|$ are the magnitudes of the principal axes. In this study, the polar angle ω indicates the angle to the y axis (east in MT) and increases from 0 to 360°. The angle ψ is defined as the normalized skew:

$$\psi = \tan^{-1}\left(\frac{\chi_{12} - \chi_{21}}{\chi_{11} + \chi_{22}}\right) \tag{A2}$$

From (A1.1) it follows that $\boldsymbol{\chi}_{ell}$ is defined as

$$\boldsymbol{\chi}_{\text{ell}} = \begin{pmatrix} \chi_a & 0 \\ 0 & \chi_b \end{pmatrix} \mathbf{R}(\psi) \tag{A3}$$

Then, the tensor in the measurement coordinate system is given by

$$\boldsymbol{\chi} = \mathbf{R}(\theta)^{-1} \begin{pmatrix} \chi_a & 0 \\ 0 & \chi_b \end{pmatrix} \mathbf{R}(\psi)\mathbf{R}(\theta) \tag{A4.1}$$

$$\boldsymbol{R}(\theta) = \begin{pmatrix} \cos\theta & \sin\theta \\ -\sin\theta & \cos\theta \end{pmatrix} \tag{A4.2}$$

With θ being the (counterclockwise) angle between the positive y axis (MT east) and the major principal axis.

In practice, the angle θ can be determined iteratively by finding the angle ω_0 so that the vector

$$\mathbf{p}(\omega_0) = \boldsymbol{\chi}\, \mathbf{c}(\omega_0 + \psi) \tag{A5}$$

is parallel to the vector $\boldsymbol{c}(\omega_0 - \psi)$ and θ equals ω_0.

Further, the magnitudes of the principal axes are calculated from (A4.1) and major and minor axes are defined as $|\chi_a|$ and $|\chi_b|$.

The circulation direction of the tensor relative to the unit circle can be derived by computing $\boldsymbol{p}(\omega)$ for two slightly increasing values of ω. Then, the signs of χ_a and χ_b are given in dependence of the circulation direction and the angle ω_0 according to Booker (2014, Table 2).

Finally, the angle α between the coordinate axis pointing positive eastward and the tensor major axis is

$$\alpha = \theta + 0.5\,\psi \tag{A6}$$

The skew β is given by

$$\beta = 0.5\,\psi \tag{A7}$$

Appendix B

The ModEM inversion code adjusts an a priori model resistivity distribution iteratively until the difference between the observations and the model theoretical responses reaches a defined minimum value. ModEM achieves this by using a numerical computation of the change in the real and imaginary parts of each element of the period-dependent observed MT tensor due to a small change in each parameter defining the

resistivity model at each iteration. A sensitivity (Jacobian) matrix, constructed from these computations, is used to update the model resistivity distribution for the next iteration. ModEM was modified to calculate the sensitivity matrix for each of the new tensors using the chain rule method for the calculation of the PT (Patro et al., 2013; Tietze et al., 2015). This is best achieved using the analytical partial derivative of each element in a (real) tensor with respect to changes in the real and imaginary parts of each element of the MT response tensor $\boldsymbol{Z} = \boldsymbol{U}+i\boldsymbol{V}$.

Real part of the apparent resistivity tensor, $\mathbf{U}_a$

$$U_{a\,1,1} = \frac{-\mu}{\omega}\left(U_{1,1}V_{2,2} + U_{2,2}V_{1,1} - 2U_{1,2}V_{1,2}\right); \quad U_{a\,1,2} = \frac{-\mu}{\omega}\left(U_{1,1}\left(V_{1,2} - V_{2,1}\right) + V_{1,1}\left(U_{1,2} - U_{2,1}\right)\right)$$

$$U_{a\,2,1} = \frac{-\mu}{\omega}\left(U_{2,2}\left(V_{2,1} - V_{1,2}\right) + V_{2,2}\left(U_{2,1} - U_{1,2}\right)\right); \quad U_{a\,2,2} = \frac{-\mu}{\omega}\left(U_{1,1}V_{2,2} + U_{2,2}V_{1,1} - 2U_{2,1}V_{2,1}\right)$$

$$\frac{\partial U_{a\,1,1}}{\partial U_{1,1}} = \frac{-\mu}{\omega}V_{2,2}; \quad \frac{\partial U_{a\,1,1}}{\partial U_{1,2}} = \frac{2\mu}{\omega}V_{1,2}; \quad \frac{\partial U_{a\,1,1}}{\partial U_{2,1}} = 0; \quad \frac{\partial U_{a\,1,1}}{\partial U_{2,2}} = \frac{-\mu}{\omega}V_{1,1}$$

$$\frac{\partial U_{a\,1,1}}{\partial V_{1,1}} = \frac{-\mu}{\omega}U_{2,2}; \quad \frac{\partial U_{a\,1,1}}{\partial V_{1,2}} = \frac{2\mu}{\omega}U_{1,2}; \quad \frac{\partial U_{a\,1,1}}{\partial V_{2,1}} = 0; \quad \frac{\partial U_{a\,1,1}}{\partial V_{2,2}} = \frac{-\mu}{\omega}U_{1,1}$$

$$\frac{\partial U_{a\,1,2}}{\partial U_{1,1}} = \frac{\mu}{\omega}\left(V_{2,1} - V_{1,2}\right); \quad \frac{\partial U_{a\,1,2}}{\partial U_{1,2}} = \frac{-\mu}{\omega}V_{1,1}; \quad \frac{\partial U_{a\,1,2}}{\partial U_{2,1}} = \frac{\mu}{\omega}V_{1,1}; \quad \frac{\partial U_{a\,1,2}}{\partial U_{2,2}} = 0$$

$$\frac{\partial U_{a\,1,2}}{\partial V_{1,1}} = \frac{\mu}{\omega}\left(U_{2,1} - U_{1,2}\right); \quad \frac{\partial U_{a\,1,2}}{\partial V_{1,2}} = \frac{-\mu}{\omega}U_{1,1}; \quad \frac{\partial U_{a\,1,2}}{\partial V_{2,1}} = \frac{\mu}{\omega}U_{1,1}; \quad \frac{\partial U_{a\,1,2}}{\partial V_{2,2}} = 0$$

$$\frac{\partial U_{a\,2,1}}{\partial U_{1,1}} = 0; \quad \frac{\partial U_{a\,2,1}}{\partial U_{1,2}} = \frac{\mu}{\omega}V_{2,2}; \quad \frac{\partial U_{a\,2,1}}{\partial U_{2,1}} = \frac{-\mu}{\omega}V_{2,2}; \quad \frac{\partial U_{a\,2,1}}{\partial U_{2,2}} = \frac{\mu}{\omega}\left(V_{1,2} - V_{2,1}\right)$$

$$\frac{\partial U_{a\,2,1}}{\partial V_{1,1}} = 0; \quad \frac{\partial U_{a\,2,1}}{\partial V_{1,2}} = \frac{\mu}{\omega}U_{2,2}; \quad \frac{\partial U_{a\,2,1}}{\partial V_{2,1}} = \frac{-\mu}{\omega}U_{2,2}; \quad \frac{\partial U_{a\,2,1}}{\partial V_{2,2}} = \frac{\mu}{\omega}\left(U_{1,2} - U_{2,1}\right)$$

$$\frac{\partial U_{a\,2,2}}{\partial U_{1,1}} = \frac{-\mu}{\omega}V_{2,2}; \quad \frac{\partial U_{a\,2,2}}{\partial U_{1,2}} = 0; \quad \frac{\partial U_{a\,2,2}}{\partial U_{2,1}} = \frac{2\mu}{\omega}V_{2,1}; \quad \frac{\partial U_{a\,2,2}}{\partial U_{2,2}} = \frac{-\mu}{\omega}V_{1,1}$$

$$\frac{\partial U_{a\,2,2}}{\partial V_{1,1}} = \frac{-\mu}{\omega}U_{2,2}; \quad \frac{\partial U_{a\,2,2}}{\partial V_{1,2}} = 0; \quad \frac{\partial U_{a\,2,2}}{\partial V_{2,1}} = \frac{2\mu}{\omega}U_{2,1}; \quad \frac{\partial U_{a\,2,2}}{\partial V_{2,2}} = \frac{-\mu}{\omega}U_{1,1}$$

Imaginary part of the apparent resistivity tensor, $\mathbf{V}_a$

$$V_{a\,1,1} = \frac{\mu}{\omega}\left(U_{1,1}U_{2,2} - V_{1,1}V_{2,2} - U_{1,2}^2 + V_{1,2}^2\right); \quad V_{a\,1,2} = \frac{\mu}{\omega}\left(U_{1,1}\left(U_{1,2} - U_{2,1}\right) + V_{1,1}\left(V_{2,1} - V_{1,2}\right)\right)$$

$$V_{a\,2,1} = \frac{\mu}{\omega}\left(U_{2,2}\left(U_{2,1} - U_{1,2}\right) + V_{2,2}\left(V_{1,2} - V_{2,1}\right)\right); \quad V_{a\,2,2} = \frac{\mu}{\omega}\left(U_{1,1}U_{2,2} - V_{1,1}V_{2,2} - U_{2,1}^2 + V_{2,1}^2\right)$$

$$\frac{\partial V_{a\,1,1}}{\partial U_{1,1}} = \frac{\mu}{\omega}U_{2,2}; \quad \frac{\partial V_{a\,1,1}}{\partial U_{1,2}} = \frac{-2\mu}{\omega}U_{1,2}; \quad \frac{\partial V_{a\,1,1}}{\partial U_{2,1}} = 0; \quad \frac{\partial V_{a\,1,1}}{\partial U_{2,2}} = \frac{\mu}{\omega}U_{1,1}$$

$$\frac{\partial V_{a\,1,1}}{\partial V_{1,1}} = \frac{-\mu}{\omega}V_{2,2}; \quad \frac{\partial V_{a\,1,1}}{\partial V_{1,2}} = \frac{2\mu}{\omega}V_{1,2}; \quad \frac{\partial V_{a\,1,1}}{\partial V_{2,1}} = 0; \quad \frac{\partial V_{a\,1,1}}{\partial V_{2,2}} = \frac{-\mu}{\omega}V_{1,1}$$

$$\frac{\partial V_{a\,1,2}}{\partial U_{1,1}} = \frac{\mu}{\omega}\left(U_{1,2} - U_{2,1}\right); \quad \frac{\partial V_{a\,1,2}}{\partial U_{1,2}} = \frac{\mu}{\omega}U_{1,1}; \quad \frac{\partial V_{a\,1,2}}{\partial U_{2,1}} = \frac{-\mu}{\omega}U_{1,1}; \quad \frac{\partial V_{a\,1,2}}{\partial U_{2,2}} = 0$$

$$\frac{\partial V_{a\,1,2}}{\partial V_{1,1}} = \frac{\mu}{\omega}\left(V_{2,1} - V_{1,2}\right); \quad \frac{\partial V_{a\,1,2}}{\partial V_{1,2}} = \frac{-\mu}{\omega}V_{1,1}; \quad \frac{\partial V_{a\,1,2}}{\partial V_{2,1}} = \frac{\mu}{\omega}V_{1,1}; \quad \frac{\partial V_{a\,1,2}}{\partial V_{2,2}} = 0$$

$$\frac{\partial V_{a\,2,1}}{\partial U_{1,1}} = 0; \quad \frac{\partial V_{a\,2,1}}{\partial U_{1,2}} = \frac{-\mu}{\omega}U_{2,2}; \quad \frac{\partial V_{a\,2,1}}{\partial U_{2,1}} = \frac{\mu}{\omega}U_{2,2}; \quad \frac{\partial V_{a\,2,1}}{\partial U_{2,2}} = \frac{\mu}{\omega}\left(U_{2,1} - U_{1,2}\right)$$

$$\frac{\partial V_{a\,2,1}}{\partial V_{1,1}} = 0; \quad \frac{\partial V_{a\,2,1}}{\partial V_{1,2}} = \frac{\mu}{\omega}V_{2,2}; \quad \frac{\partial V_{a\,2,1}}{\partial V_{2,1}} = \frac{-\mu}{\omega}V_{2,2}; \quad \frac{\partial V_{a\,2,1}}{\partial V_{2,2}} = \frac{\mu}{\omega}\left(V_{1,2} - V_{2,1}\right)$$

$$\frac{\partial V_{a\,2,2}}{\partial U_{1,1}} = \frac{\mu}{\omega}U_{2,2}; \quad \frac{\partial V_{a\,2,2}}{\partial U_{1,2}} = 0; \quad \frac{\partial V_{a\,2,2}}{\partial U_{2,1}} = \frac{-2\mu}{\omega}U_{2,1}; \quad \frac{\partial V_{a\,2,2}}{\partial U_{2,2}} = \frac{\mu}{\omega}U_{1,1}$$

$$\frac{\partial V_{a\,2,2}}{\partial V_{1,1}} = \frac{-\mu}{\omega}V_{2,2}; \quad \frac{\partial V_{a\,2,2}}{\partial V_{1,2}} = 0; \quad \frac{\partial V_{a\,2,2}}{\partial V_{2,1}} = \frac{2\mu}{\omega}V_{2,1}; \quad \frac{\partial V_{a\,2,2}}{\partial V_{2,2}} = \frac{-\mu}{\omega}V_{1,1}$$

Apparent resistivity phase tensor, $\boldsymbol{\phi}_a = \boldsymbol{U}_a^{-1}\boldsymbol{V}_a$

$$
\begin{aligned}
\Phi_{a\,1,1} &= -K\Big(\big(U_{1,1}V_{2,2}+U_{2,2}V_{1,1}-2U_{2,1}V_{2,1}\big)\Big(U_{1,1}U_{2,2}-V_{1,1}V_{2,2}-U_{1,2}^2+V_{1,2}^2\Big)\\
&\quad -\big(U_{1,1}\big(V_{1,2}-V_{2,1}\big)+V_{1,1}\big(U_{1,2}-U_{2,1}\big)\big)\big(U_{2,2}\big(U_{2,1}-U_{1,2}\big)+V_{2,2}\big(V_{1,2}-V_{2,1}\big)\big)\Big)\\
\Phi_{a\,1,2} &= -K\big(\big(U_{1,1}V_{2,2}+U_{2,2}V_{1,1}-2U_{2,1}V_{2,1}\big)\big(U_{1,1}\big(U_{1,2}-U_{2,1}\big)+V_{1,1}\big(V_{2,1}-V_{1,2}\big)\big)\\
&\quad -\big(U_{1,1}\big(V_{1,2}-V_{2,1}\big)+V_{1,1}\big(U_{1,2}-U_{2,1}\big)\big)\Big(U_{1,1}U_{2,2}-V_{1,1}V_{2,2}-U_{2,1}^2+V_{2,1}^2\Big)\Big)\\
\Phi_{a\,2,1} &= -K\,\big(\big(U_{1,1}V_{2,2}+U_{2,2}V_{1,1}-2U_{1,2}V_{1,2}\big)\big(U_{2,2}\big(U_{2,1}-U_{1,2}\big)+V_{2,2}\big(V_{1,2}-V_{2,1}\big)\big)\\
&\quad -\big(U_{2,2}\big(V_{2,1}-V_{1,2}\big)+V_{2,2}\big(U_{2,1}-U_{1,2}\big)\big)\Big(U_{1,1}U_{2,2}-V_{1,1}V_{2,2}-U_{1,2}^2+V_{1,2}^2\Big)\Big)\\
\Phi_{a\,2,2} &= -K\,\Big(\big(U_{1,1}V_{2,2}+U_{2,2}V_{1,1}-2U_{1,2}V_{1,2}\big)\Big(U_{1,1}U_{2,2}-V_{1,1}V_{2,2}-U_{2,1}^2+V_{2,1}^2\Big)\\
&\quad -\big(U_{2,2}\big(V_{2,1}-V_{1,2}\big)+V_{2,2}\big(U_{2,1}-U_{1,2}\big)\big)\big(U_{1,1}\big(U_{1,2}-U_{2,1}\big)+V_{1,1}\,\big(V_{2,1}-V_{1,2}\big)\big)\Big)\\
K &= \frac{1}{\det(U_a)} = \frac{1}{H\big(U_{ij}V_{ij}\big)}
\end{aligned}
$$

The term K is therefore a function (only) of the real and imaginary parts of $\boldsymbol{Z}$ so that expressions for the partial derivatives of $\boldsymbol{\phi}_a$ must be calculated using the quotient rule for differentiation. The partial derivative of, for example, $\phi_{a\,1,1}$ with respect to $U_{1,1}$ may be written as $F' = (HG' - GH')/H^2$ for $F = G/H$, where G and H can be written as $(ax+b)(cx+d) - (ex+f)(gx+h)$, a,b,c,d,e, f, g, and h are constants, and $x = U_{11}$.The partial derivatives of G and H are $2(ac - eg)x+(ad+bc - eh - fg)$. The calculation of the partial derivative of $\phi_{a\,1,1}$ proceeds as follows:

$$
\begin{aligned}
G &= \big(U_{1,1}V_{2,2}+U_{2,2}V_{1,1}-2U_{2,1}V_{2,1}\big)\Big(U_{1,1}U_{2,2}-V_{1,1}V_{2,2}-U_{1,2}^2+V_{1,2}^2\Big)\\
&\quad -\big(U_{1,1}\big(V_{1,2}-V_{2,1}\big)+V_{1,1}\big(U_{1,2}-U_{2,1}\big)\big)\big(U_{2,2}\big(U_{2,1}-U_{1,2}\big)+V_{2,2}\big(V_{1,2}-V_{2,1}\big)\big)\\
a &= V_{2,2}; \qquad b = U_{2,2}V_{1,1}-2U_{2,1}V_{2,1}; \quad c = U_{2,2}; \qquad d = -V_{1,1}V_{2,2}-U_{1,2}^2+V_{1,2}^2\\
e &= V_{1,2}-V_{2,1}; \qquad f = V_{1,1}\big(U_{1,2}-U_{2,1}\big); \qquad g = 0; \qquad h = U_{2,2}\big(U_{2,1}-U_{1,2}\big)+V_{2,2}\big(V_{1,2}-V_{2,1}\big)\\
G' &= 2(ac-eg)\mathrm{x}+(ad+bc-eh-fg) \qquad = 2V_{2,2}U_{2,2}U_{1,1}+V_{2,2}\Big(-V_{1,1}V_{2,2}-U_{1,2}^2+V_{1,2}^2\Big)\\
&\quad +\big(U_{2,2}V_{1,1}-2U_{2,1}V_{2,1}\big)U_{2,2}-\big(V_{1,2}-V_{2,1}\big)\big(U_{2,2}\big(U_{2,1}-U_{1,2}\big)+V_{2,2}\big(V_{1,2}-V_{2,1}\big)\big)\\
H &= \big(U_{1,1}V_{2,2}+U_{2,2}V_{1,1}-2U_{1,2}V_{1,2}\big)\big(U_{1,1}V_{2,2}+U_{2,2}V_{1,1}-2U_{2,1}V_{2,1}\big)\\
&\quad -\big(U_{1,1}\big(V_{1,2}-V_{2,1}\big)+V_{1,1}\big(U_{1,2}-U_{2,1}\big)\big)\big(U_{2,2}\big(V_{2,1}-V_{1,2}\big)+V_{2,2}\big(U_{2,1}-U_{1,2}\big)\big)\\
a &= V_{2,2}; \qquad b = U_{2,2}V_{1,1}-2U_{1,2}V_{1,2}; \quad c = V_{2,2}; \qquad d = U_{2,2}V_{1,1}-2U_{2,1}V_{2,1}\\
e &= V_{1,2}-V_{2,1}; \qquad f = V_{1,1}\big(U_{1,2}-U_{2,1}\big); \qquad g = 0; \qquad h = U_{2,2}\big(V_{2,1}-V_{1,2}\big)+V_{2,2}\big(U_{2,1}-U_{1,2}\big)\\
H' &= 2(ac-\mathrm{eg})x+(ad+bc-eh-fg) \qquad = 2V_{2,2}^2U_{1,1}+V_{2,2}\big(U_{2,2}V_{1,1}-2U_{2,1}V_{2,1}\big)\\
&\quad +\big(U_{2,2}V_{1,1}-2U_{1,2}V_{1,2}\big)V_{2,2}-\big(V_{1,2}-V_{2,1}\big)\big(U_{2,2}\big(V_{2,1}-V_{1,2}\big)+V_{2,2}\big(U_{2,1}-U_{1,2}\big)\big)\\
\frac{\partial\phi_{\mathrm{a}\,1,1}}{\partial U_{1,1}} &= \frac{HG'-GH'}{H^2}
\end{aligned}
$$

B1. Tensor Element Errors

The sensitivities of the tensor elements above are prerequisites for the calculation of their errors from errors in MT tensor observations. A preliminary study of 3-D models indicates that assuming that covariance between the real and imaginary MT tensor elements is zero, errors estimated for $\boldsymbol{U_a}$ and $\boldsymbol{V_a}$ tensors may be >20% larger than errors estimated using the full covariance in the delta method; they are often much larger for $\boldsymbol{\phi_a}$ and $\boldsymbol{\phi}$ tensors.

Acknowledgments
Colin Brown was supported by the Griffith Geoscience Award from the Department of Communications, Energy and Natural Resources under the National Geoscience Programme 2007–2013. The views and recommendations contained in this study reflect the views of the authors and do not necessarily reflect the views and opinions of the Irish Minister for Communications, Energy and Natural Resources. The results are all based on synthetic studies, and no data have been used. The reviews by two anonymous reviewers and the comments from Max Moorkamp significantly improved the manuscript. Open access funding enabled and organized by Projekt Deal.

References

Bibby, H. M. (1986). Analysis of multiple-source bipole-dipole resistivity surveys using the apparent resistivity tensor. *Geophysics*, *51*(4), 972–983. https://doi.org/10.1190/1.1442155

Bibby, H. M., Caldwell, T. G., & Brown, C. (2005). Determinable and non-determinable parameters of galvanic distortion in magnetotellurics. *Geophysical Journal International*, *163*(3), 915–930. https://doi.org/10.1111/j.1365-246X.2005.02779.x

Booker, J. R. (2014). The magnetotelluric phase tensor: A critical review. *Surveys in Geophysics*, *35*(1), 7–40. https://doi.org/10.1007/s10712-013-9234-2

Brown, C. (2016). Magnetotelluric tensors, electromagnetic field scattering and distortion in three-dimensional environments. *Journal of Geophysical Research: Solid Earth*, *121*, 7040–7053. https://doi.org/10.1002/2016JB013035

Caldwell, T. G., & Bibby, H. M. (1998). The instantaneous apparent resistivity tensor: A visualisation scheme for LOTEM electric field measurements. *Geophysical Journal International*, *135*(3), 817–834. https://doi.org/10.1046/j.1365-246X.1998.00668.x

Caldwell, T. G., Bibby, H. M., & Brown, C. (2002). Controlled-source apparent resistivity tensors and their relationship to the magnetotelluric impedance tensor. *Geophysical Journal International*, *151*(3), 755–770. https://doi.org/10.1046/j.1365-246X.2002.01798.x

Caldwell, T. G., Bibby, H. M., & Brown, C. (2004). The magnetotelluric phase tensor. *Geophysical Journal International*, *158*(2), 457–469. https://doi.org/10.1111/j.1365-246X.2004.02281.x

Cembrowski, M., & Junge, A. (2018). Electrical anisotropy in the presence of oceans—A sensitivity study. *Geophysical Journal International*, *213*(2), 1029–1043. https://doi.org/10.1093/gji/ggy044

Chave, A. D., & Smith, J. T. (1994). On electric and magnetic galvanic distortion tensor decompositions. *Journal Geophysical Research*, *99*(B3), 4669–4682. https://doi.org/10.1029/93JB03368

Dekker, D. L., & Hastie, L. M. (1980). Magneto-telluric impedances of an anisotropic layered earth model. *Geophysical Journal of the Royal Astronomical Society*, *61*(1), 11–20. https://doi.org/10.1111/j.1365-246X.1980.tb04300.x

Efron, B. (1982). *The jackknife, the bootstrap and other resampling plans. CMMS-NSF Regional Conference*, *Series in Applied Mathematics*. Philadelphia: Society for industrial and applied Mathematics (SIAM). ISBN: 978-0-898711-79-0. https://doi.org/10.101137/1.978161197039.ch6

Egbert, G. D., & Kelbert, A. (2012). Computational recipes for electromagnetic inverse problems. *Geophysical Journal International*, *189*(1), 251–267. https://doi.org/10.1111/j.1365-246X.2011.05347.x

González-Castillo, L., Galindo-Zaldivar, J., Junge, A., & Martinez-Moreno, F. J. (2015). Evidence of a large deep conductive body within the basement of the Guadalquivir foreland Basin (Betic Cordillera, S-Spain) from tipper vector modelling: Tectonic implications. *Tectonophysics*, *663*, 354–363. https://doi.org/10.1016/j.tecto.2015.08.013

Groom, R. W., & Bailey, R. C. (1989). Decomposition of magnetotelluric impedance tensors in the presence of local three-dimensional galvanic distortion. *Journal of Geophysical Research*, *94*(B2), 1913–1925. https://doi.org/10.1029/JB094iB02p01913

Häuserer, M., & Junge, A. (2011). Electrical mantle anisotropy and crustal conductor: A 3-D conductivity model of the Rwenzori Region in western Uganda. *Geophysical Journal International*, *185*(3), 1235–1242. https://doi.org/10.1111/j.1365-246X.2011.05006.x

Heise, W., Caldwell, T. G., Bibby, H. M., & Bannister, S. C. (2008). Three-dimensional modelling of magnetotelluricdata from the Rotokawa geothermal field, Taupo Volcanic Zone. New Zealand. *Geophysical Journal International*, *173*(2), 740–750. https://doi.org/10.1111/j.1365-246X.2008.03737.x

Jiracek, G. R. (1990). Near-surface and topographic distortions in electromagnetic induction. *Surveys in Geophysics*, *11*(2-3), 163–203. https://doi.org/10.1007/BF01901659

Jones, F. W., & Price, A. T. (1970). The perturbations of alternating geomagnetic fields by conductivity anomalies. *Geophysical Journal International*, *20*(3), 317–334. https://doi.org/10.1111/j.1365-246X.1970.tb06073.x

Kaufman, A. A. (1985). Tutorial: Distribution of alternating electrical charges in a conducting medium. *Geophysical Prospecting*, *33*(2), 171–184. https://doi.org/10.1111/j.1365-2478.1985.tb00427.x

Kaufman, A. A., & Keller, G. V. (1981). The magnetotelluric sounding method. In *Methods in Geochemistry and Geophysics* (Vol. 15, p. 595). Amsterdam: Elsevier Science Limited. ISBN-13: 978-0444418630

Kelbert, A., Egbert, G. D., & deGroot Hedlin, C. (2012). Crust and upper mantle electrical conductivity beneath the Yellowstone Hotspot Track. *Geology*, *40*(5), 447–450. https://doi.org/10.1130/G32655.1

Kelbert, A., Meqbel, N., Egbert, G. D., & Tandon, K. (2014). ModEM: A modular system for inversion of electromagnetic geophysical data. *Computers & Geosciences*, *66*, 40–53. https://doi.org/10.1016/j.cageo.2014.01.010

Ledo, J. (2006). 2-D versus 3-D magnetotelluric data interpretation. *Surveys in Geophysics*, *27*(1), 111–148. https://doi.org/10.1007/s10712-006-0002-4

Li, Y., & Oldenburg, D. W. (1991). Aspects of charge accumulation in d.c. resistivity experiments. *Geophysical Prospecting*, *39*(6), 803–826. https://doi.org/10.1111/j.1365-2478.1991.tb00345.x

Löwer, A. (2014). Magnetotellurische Erkundung geologischer Großstrukturen des südwestlichen Vogelsberges mit anisotroper, dreidimensionaler—Modellierung der Leitfähigkeitsstrukturen. *Dissertation*, Goethe Universität Frankfurt.

Löwer, A., & Junge, A. (2017). Magnetotelluric transfer functions: Phase tensor and tipper vector above a simple anisotropic three-dimensional conductivity anomaly and implications for 3D isotropic inversion. *Pure and Applied Geophysics*, *174*(5), 2089–2101. https://doi.org/10.1007/s00024-016-1444-3

Martí, A. (2014). The role of electrical anisotropy in magnetotelluric responses: From modelling and dimensionality analysis to inversion and interpretation. *Surveys in Geophysics*, *35*(1), 179–218. https://doi.org/10.1007/s10712-013-9233-3

Meqbel, N., Weckmann, U., Muñoz, G., & Ritter, O. (2016). Crustal metamorphic fluid flux beneath the Dead Sea Basin: Constraints from 2D and 3D magnetotelluric modelling. *Geophysical Journal International*, *207*(3), 1609–1629. https://doi.org/10.1093/gji/ggw359

Miensopust, M. P. (2017). Application of 3-D electromagnetic inversion in practice: Challenges, pitfalls and solution approaches. *Surveys in Geophysics*, *38*(5), 869–933. https://doi.org/10.1007/s10712-017-9435-1

Moorkamp, M. (2007). Comment on "The magnetotelluric phase tensor" by T. Grant Caldwell, Hugh M. Bibby and Colin Brown. *Geophysical Journal International*, *171*(2), 565–566. https://doi.org/10.1111/j.1365-246X.2007.03490.x

Park, S. K. (1985). Distortion of magnetotelluric sounding curves by three-dimensional structures. *Geophysics*, *50*(5), 785–797. https://doi.org/10.1190/1.1441953

Patro, P. K., Uyeshima, M., & Siripunvaraporn, W. (2013). Three-dimensional inversion of magnetotelluric phase tensor data. *Geophysical Journal International*, *192*(1), 58–66. https://doi.org/10.1093/gji/ggs014

Pek, J., & Santos, F. A. M. (2002). Magnetotelluric impedances and parametric sensitivities for 1-D anisotropic layered media. *Computers & Geosciences*, *28*(8), 939–950. https://doi.org/10.1016/S0098-3004(02)00014-6

Schmucker, U. (1987). Substitute conductors for electromagnetic response estimates. *Pure and Applied Geophysics*, *125*(2-3), 341–367. https://doi.org/10.1007/BF00874501

Siripunvaraporn, W., & Egbert, G. (2000). An efficient data-subspace inversion method for 2-D magnetotelluric data. *GEOPHYSICS*, *65*(3), 791–803. https://doi.org/10.1190/1.1444778

Tietze, K., & Ritter, O. (2013). Three-dimensional magnetotelluric inversion in practice-the electrical conductivity structure of the San Andreas Fault in Central California. *Geophysical Journal International*, *195*(1), 130–147. https://doi.org/10.1093/gji/ggt234

Tietze, K., Ritter, O., & Egbert, G. D. (2015). 3-D joint inversion of the magnetotelluric phase tensor and vertical magnetic transfer functions. *Geophysical Journal International*, *203*(2), 1128–1148. https://doi.org/10.1093/gji/ggv347

Vozoff, K. (1986). *Magnetotelluric methods*, *Geophysics Reprint Series* (Vol. 5). Society of Exploration Geophysicists: Tulsa, Okla.

Weckmann, U., Ritter, O., & Haak, V. (2003). Images of the magnetotelluric apparent resistivity tensor. *Geophysical Journal International*, *155*(2), 456–468. https://doi.org/10.1046/j.1365-246X.2003.02062.x